SCUOLA NORMALE SUPERIORE

PH.D. THESIS

IN

BIOPHYSICAL SCIENCES

Fingerprinting dynamic subcellular nanostructures by spatiotemporal correlation spectroscopy: the lysosome case

William Durso

ADVISOR

Prof. Francesco Cardarelli

2021/22

Table of Contents

Foreword **6**

CHAPTER 1 ..... **10**

1. Introduction **10**

1.1 Transmission Electron Microscopy (TEM) 12

1.2 Super Resolution Fluorescence Microscopy (SRFM) by single-molecule localization 14

1.3 Stimulated Emission Depletion (STED) 18

1.4 Single Particle Tracking (SPT) 20

1.5 Fluctuation-based techniques 23

1.5.1 Fluorescence Correlation Spectroscopy (FCS) 23

1.5.2 Extending FCS to the spatial dimension: scanning-FCS and Raster Image Correlation Spectroscopy (RICS) 24

1.5.3 Phasor analysis of Local Image Correlation Spectroscopy (PLICS): recovering spatial information at the sub-cellular scale 27

1.5.4 Joining spatial and temporal information: Spatiotemporal Image Correlation Spectroscopy (STICS) and image-derived Mean Square Displacement (*i*MSD) 28

CHAPTER 2 ..... **32**

2. *i*MSD: from molecular to sub-celluar scale **32**

2.1 Image-derived MSD (*i*MSD) analysis on molecular scale 32

2.2 Image processing and data analysis 35

2.3 *i*MSD analysis: from molecules to sub-cellular nanostructures 38

2.4 The role of the time window: super-diffusive or sub-diffusive lysosomes? 42

2.5 The dynamic fingerprint of intracellular structures 48

2.6 The dynamic fingerprint of the endosome-lysosome pathway 53

2.7 The 'strange' case of the evolving macropinosome 55

CHAPTER 3 59

3. Probing labeling-induced alteration of lysosome structural/dynamic properties by *i*MSD 59

3.1 *i*MSD detects structural and dynamic alterations of lysosome induced by labelling 60

3.2 Correlation between marker expression and lysosome size 69

CHAPTER 4 75

4. Lysosome structural and dynamic properties during NSCs differentiation 75

4.1 The biological system 77

4.2 iMSD analysis of lysosome dynamics during NSCs differentiation 79

4.3 SPT analysis of lysosome motion during NSCs differentiation 91

4.4 Conclusions 99

CHAPTER 5 ..... **103**

5. Conclusions and future perspectives **103**

APPENDIX **115**

I. Materials and Methods **115**

i. Cell culture and treatments 115

ii. Plasmids and cell transfections 119

iii. Live cell imaging 121

Bibliography **124**

Foreword

A distinguishing feature of eukaryotic cells at the sub-cellular spatial scale is that of being organized into membrane-enclosed, sub-micrometric, and dynamic organelles or compartments, such as endocytic/secretory vesicles, early-late endosomes, lysosomes, mitochondria, etc. [1]. As testified, among others, by the 2013 Nobel Prizes in Physiology or Medicine [2], such structures are pivotal in determining how cells shuttle proteins and other biomolecules from one location to another, thus emerging as a legitimate platform for cell signaling regulation [3]. The overall picture is that a tight regulation of their size/morphology and trafficking properties determines how cells are able to comply with internal or external stimuli both in the physiological and in the pathological conditions [4–6]. We now know that disturbances in this transport system have deleterious effects that can contribute to neurologic diseases including autism [7] and schizophrenia [8], as well as to diabetes [9], immunologic [10] and hematologic disorders [11].

In spite of the huge research efforts, retrieving quantitative, simultaneous access to both structural and dynamic information on such tiny subcellular structures remains a challenge in the field. If

electron microscopy (EM)-based analysis was pivotal to probe the finest (ultra)structural details of many sub-cellular structure, that was inevitably done at the expense of dynamic information. On the other hand, standard optical microscopy tools shed new light onto the organelles dynamic behavior and their regulation [12–14], but typically underexploited the spatial dimension and, as a consequence, the structural information. To tackle these limitations, our group recently proposed a fluctuation-based analytical tool (named imaging-derived Mean Square Displacement, or *i*MSD) that is able to simultaneously extract both structural and dynamic average parameters of the target object from simple time-lapse imaging, with no a-priori knowledge on the system, no need to extract trajectories, no need for complex labelling, and in live cells [15]. Thanks to this approach, large-scale fingerprinting of dynamic structures can be achieved, in a fast and robust way, at the whole-cell-population level.

Thus far, *i*MSD technique has only been applied to molecules [16] and gene-delivery nanoparticles [17]. The Aim of this work is to extend the application of this method to one of the natural conditions of living matter at the sub-cellular spatial scale, that of sub-micrometric, dynamic structures or compartments deputed to shuttle molecules around the cell.

For the sake of clearness, the main results of this Thesis were divided into separate Chapters as follow:

- In ***Chapter 1***, a review of the more common imaging-based techniques developed to observe subcellular structures at high spatial and temporal resolution is presented, with a particular focus on their ability to retrieve the dynamic and structural properties of the biological objects of interest.

- In ***Chapter 2*** the imaging-derived mean square displacement (*i*MSD) method is introduced, with a particular focus on its application to study the dynamic and structural properties of subcellular organelles. A unique triplet of average parameters (diffusivity, anomalous coefficient and size), extracted from each *i*MSD and represented in a 3D parametric space, define the so called "dynamic fingerprint".

- In ***Chapter 3*** alterations of structural and dynamic properties of lysosome, caused by labeling strategies and/or procedures, are probed using *i*MSD. In particular, it is shown how Lipofectamine reagents, commonly used to transiently transfect lysosome markers fused to fluorescent proteins,

irreversibly alter the organelle structural and dynamic identity.

- In ***Chapter 4***, the lysosome structural and dynamic properties are investigated during the process of differentiation of neuronal stem cells (NSCs) obtained from mouse embryonic stem cells (mESCs) by means of *i*MSD and single particle tracking (SPT). Here *i*MSD is used to analyze the average dynamic behavior of lysosomal population in the cell soma during the differentiation process. SPT, instead, by extracting the trajectories of single lysosomes, allowed to properly characterized the organelle motion in all districts, including the projections of the differentiating cell.

- In ***Chapter 5***, in conclusion of this Work, possible implementations to improve the performances of *i*MSD approach are discussed, together with potential future applications of the method in biophysics and related fields.

CHAPTER 1

1. Introduction

Membrane-enclosed, sub-micrometric, and dynamic organelles or compartments, such as endocytic/secretory vesicles, early-late endosomes, lysosomes, mitochondria, etc. are emerging as a hub for cell-signaling regulation [1,3]. The idea that a finely tuned regulation of their structural (e.g. size/morphology) and dynamic (e.g. diffusivity, mode of motion) properties determines how cells comply with internal or external stimuli, is supported by consolidated scientific literature [4–6]. As a consequence, it is not surprising that average alterations of the same properties are typically found as hallmarks of pathological conditions: derailed endocytosis commonly found in cancer cells [4,5], altered granule trafficking is found in β-cells exposed to Type-2-Diabetes-mimicking conditions [18], enlarged lysosomes packed with twisted microtubules observed in globoid cell leukodystrophy or galactosylceramide lipidosis [19], abnormalities in the endosomal-lysosomal system occurring in neurodegenerative diseases, especially Alzheimer's disease (AD) [20], are just few examples.

Concerning structural information, current knowledge mostly owes to transmission electron microscopy (TEM) analysis. Unfortunately, however, the peculiar nanoscale spatial accuracy of TEM is achieved at the expenses of the dynamic information, which is inevitably lost. On the other hand, the recent advances in live-cell imaging technologies, including development of specific fluorescent markers, optimization of labeling protocols, and availability of ever more sensitive and less invasive optical microscopes potentially open the way to the study of structural and dynamic properties at the nano-micro scale and in live cells. For instance, well established analytical tools are at our disposal to extract the relevant structural (e.g. size by phasor analysis of local image correlation spectroscopy, PLICS [21]) or dynamic (e.g. diffusion law by SPT [22–27]) parameters at the sub-cellular scale. In the next sub-chapters the main imaging-based techniques developed to observe organelles and subcellular nanostructures at high spatial and temporal resolution will be reviewed. In particular, the balance between dynamic and structural information will be examined.

1.1 Transmission Electron Microscopy (TEM)

For over 60 years, transmission electron microscopy (TEM) has been a unique method to investigate cell organelles morphology and essential to probe the finest ultrastructural details of many sub-cellular structure. For example, TEM images revealed that insulin granules contains an electron-dense core separated from the surrounding membrane by a characteristic halo (**Figure 1.1**), composed by the semi-crystal structure made by hexamers of mature insulin molecules [28].

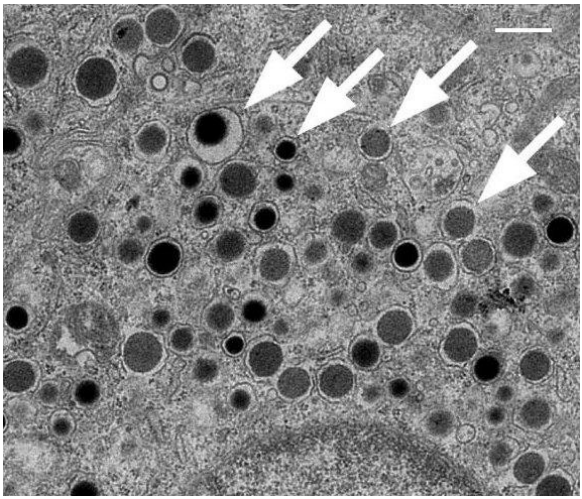

Figure 1.1 TEM image of a rat beta cell*. Insulin granules are indicated by white arrows. Scale bar: 1 µm. Image adapted from ref.* [29]

Conventional EM that involves chemical fixation of cells and tissues, dehydration, embedding in resins, and ultrathin sectioning is the method of choice to appreciate these ultrastructural details (**Figure 1.2**) [30].

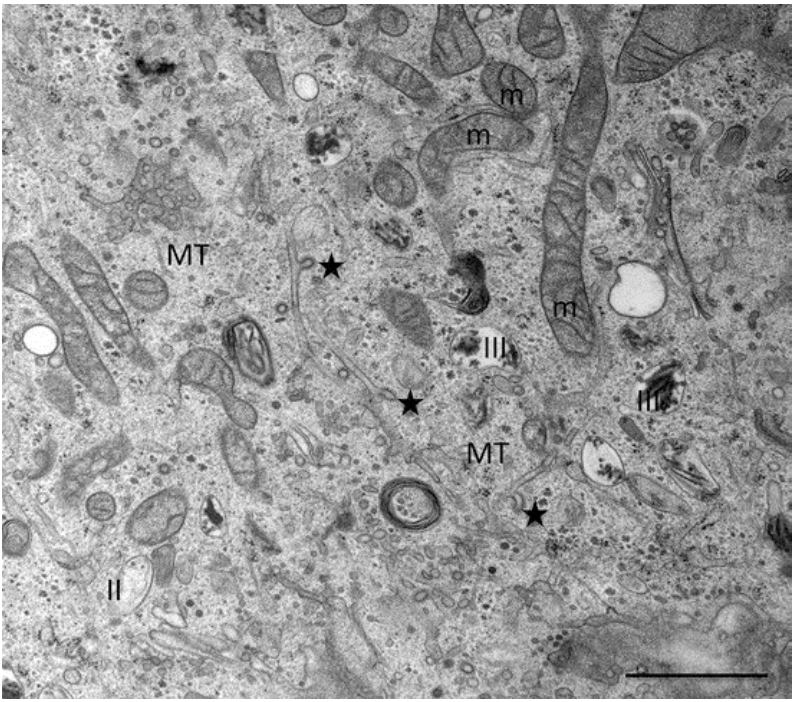

Figure 1.2 Example of TEM image of a cell. *Different organelles are clearly visible and well preserved: mitochondria (m), microtubules (MT), melanosomes stage II (II) and stage III (III), and the endosomal network depicting clathrin-coated buds (star-mark). High pressure frozen MNT1 cells. Scale bar: 1 μm. Image reprinted from ref.* [30]

Two main categories of optical microscopy methodologies actually push the spatial resolution beyond the diffraction limit set by Ernst Abbe's equation [31]: single-molecule localization (SML) such as stochastic optical localization microscopy (STORM) and photoactivated localization microscopy (PALM), and stimulated emission depletion (STED).

1.2 Super Resolution Fluorescence Microscopy (SRFM) by single-molecule localization

In a typical fluorescently labelled biological sample, where multiple molecules are present in close proximity, localization becomes inaccurate or impossible as the images of these fluorophores overlap. By switching between an active and dark state a small amount of fluorophores, molecules within a diffraction limited region can be activated at different time points so that they can be individually imaged, localized, and subsequently deactivated (the general principle is explained in **Figure 1.3**). These approaches were named stochastic optical localization microscopy (STORM) [32], photoactivated localization microscopy (PALM) [33] and fluorescence photoactivation localization microscopy (fPALM) [34].

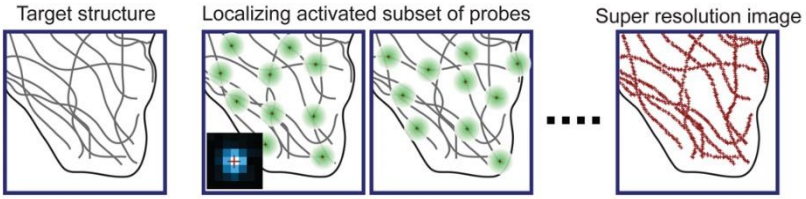

Figure 1.3 The principle of SRFM by single molecule localization. *Different fluorescent probes marking the sample structure are activated at different time points, allowing subsets of fluorophores to be imaged and localized to high precision. Iterating the activation and imaging process many fluorescent probes are localized and a super-resolved image is generated. Image reprinted from ref.* [35]

Figure 1.4 shows STORM images of clathrin-coated pits (CCPs) in BS-C-1 cells. When imaged by conventional fluorescence microscopy, all CCPs appeared as nearly diffraction-limited spots with no discernible structure. In STORM images the round shape of CCPs was clearly seen (**Figure 1.4B** and **D**). The size distribution of CCPs measured from the 2D projection image, 180 ± 40 nm, agrees quantitatively with the size distribution determined using electron microscopy [36].

Although these super-resolution approach relay on wide-field imaging methods, the imaging speed is limited by the time required to accumulate a fluorophore localization density that is sufficient for a desired resolution. Since different subsets of fluorescent probes are localized sequentially, a large number of imaging frames (typically

5,000–40,000 frames, **Figure 1.5**) and up to several minutes of time are needed to reconstruct the final super-resolved image [37].

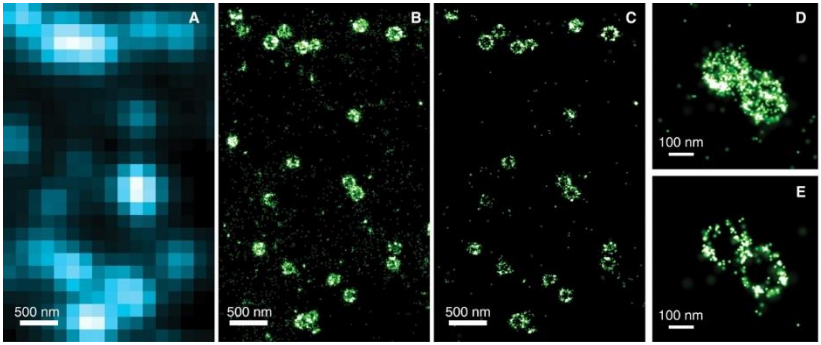

Figure 1.4 Three-dimensional STORM imaging of clathrin-coated pits in a cell. *(**A**) Conventional direct immunofluorescence image of clathrin in a region of a BS-C-1 cell. (**B**) The 2D STORM image of the same area, with all localizations at different z positions included. (**C**) An x-y cross section (50 nm thick in z) of the same area, showing the ring-like structure of the periphery of the CCPs at the plasma membrane. (**D** and **E**) Magnified view of two nearby CCPs in 2D STORM (D) and their x-y cross section (100 nm thick) in the 3D image (E). Image adapted from ref.* [36]

Many cellular processes (included those related to the subcellular organelles dynamics which are of interest here) take place on a much shorter timescale [38,39] and require a large amount of photons to be delivered on the sample. In most common applications, these techniques require fixed samples, analogously to TEM.

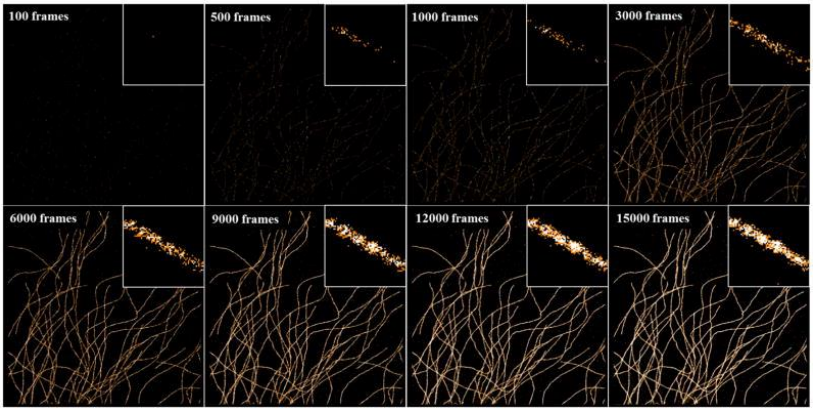

Figure 1.5 STORM images of microtubules immuno-stained by Alexa Fluor 647 reconstructed by different numbers of imaging frames. *The insets show the magnified region. Image reprinted from ref.* [37]

However, several important implementations have the potential to reveal the nanoscale dynamic behavior of single molecules directly within living samples. For instance, in the context of SML methods, by combining PALM with single-particle tracking (SPT), one can build mobility maps by measuring the trajectories of many individual molecules at the same time [40].

1.3 Stimulated Emission Depletion (STED)

STED was proposed by Hell and colleagues in 1994 [41] as a technique capable to provide sub-diffraction resolution. The principle of this approach relies on the reduction of effective PSF. This has been achieved by selectively suppressing fluorescence photon emission from the outside edge of the excitation laser beam scanning the sample with a second laser having a doughnut shape. The STED laser beam also has a red-shifted emission wavelength in order to match the energy difference between the ground and excited state of stimulated emission. **Figure 1.6** shows live neurons imaged with STED nanoscopy, visualizing sub-diffraction spaced periodic structures of actin.

Moreover, combining STED with fluorescence correlation spectroscopy (FCS), diffraction-unlimited imaging has the potential to reveal protein dynamics moving in the plasma membrane. STED-FCS experiments have shown that diffusion speeds of lipid are heterogeneously distributed in the plasma membrane of different living cells [42].

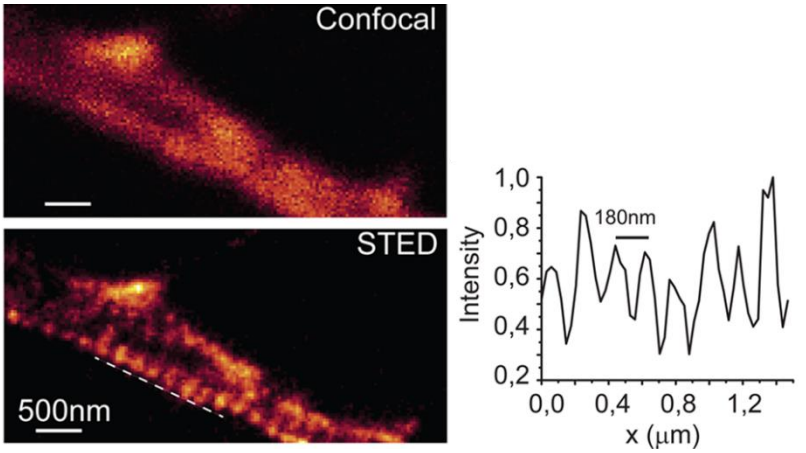

Figure 1.6 STED image (bottom) of live hippocampal primary neurons (grown for 6 days in vitro.). *(Right) Line profile along the dendrite (white dashed line) showing periodic cytoskeletal actin structures with a period of ~180 nm. Image adapted from ref.* [43]

A recently proposed approach combines STED imaging with ultrafast scanning techniques, in order to render STED nanoscopy temporally stochastic. In confocal microscopes, when a pixel dwell times is set into the range of microseconds, fluorophores typically undergo from 10 to 1,000 excitation events until the illumination spot is moved. Using the electro-optical scanning technology, Schneider and co-workers, were able to ultrafast scan with a line-scanning frequency of 250 kHz, delivering a number of consecutive excitation pulses of the fluorophore per scan cycle down to one or two pulses in one-

dimensional (1D) and 8–10 pulses in 2D scanning [44]. Using single particle tracking (SPT) and taking advantage of the 70-nm static spatial resolution provided by STED, these authors investigated the dynamics of fluorescently labeled vesicles (**Figure 1.7**) in living Drosophila or HIV-1 particles in cells with a temporal resolution of 5–10 ms [44].

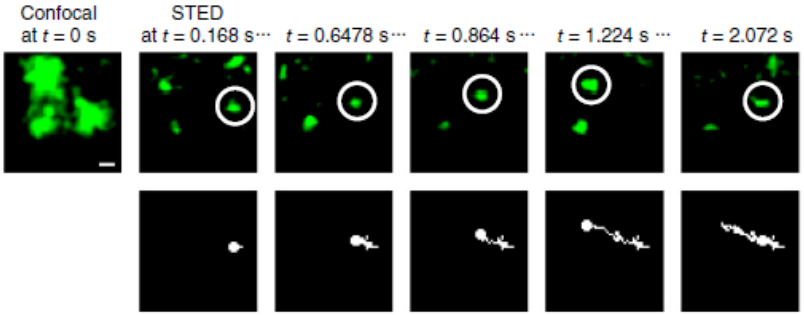

Figure 1.7 STED imaging of millisecond-scale dynamic processes. *Live STED imaging of EGFP-labeled vesicles in neuron of Drosophila larvae with a temporal resolution of 8 ms (125 f.p.s.). Scale bar: 200 nm. Image adapted from ref.* [44]

1.4 Single Particle Tracking (SPT)

Single Particle Tracking (SPT) is an imaging technique able to locate and reconstruct the trajectory of a diffusing object with nanometer precision. SPT also provides access to single molecule behavior in the

natural context of living cells, thereby allowing a complete statistical characterization of the system under study. The use of a nanoscopic reporter (gold nanoparticle, QD or fluorescence molecule) attached to the biomolecule of interest allows to image its motion by optical microscopy. The analysis performed using several images processing techniques or software generate the resulting trajectories and provide access to all the dynamics parameter such as mean square displacements, diffusion, velocity, etc. as a function of time and space. The principle of SPT is schematically described in **Figure 1.8** [45].

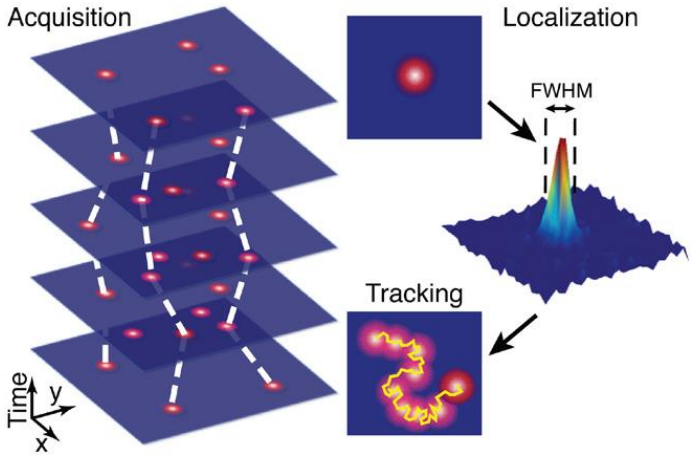

Figure 1.8 Schematic representation of SPT workflow. *An images stack is obtained from fast recording of a reporter. For each image of the time series the detected spots are localized based on the center of mass. Linking the spot positions of each*

corresponding spots for all the time series, the trajectories that describe the motion of the single particles are generated. Image reprinted from ref. [45]

SPT finds several applications in biology where following the dynamics of processes at the nanoscale can be of crucial importance (e.g. diffusion law by SPT [22–27]). **Figure 1.9** shows a SPT application to a fluorescently labelled organelle (lysosome) combined to super-resolution imaging (i.e. STORM).

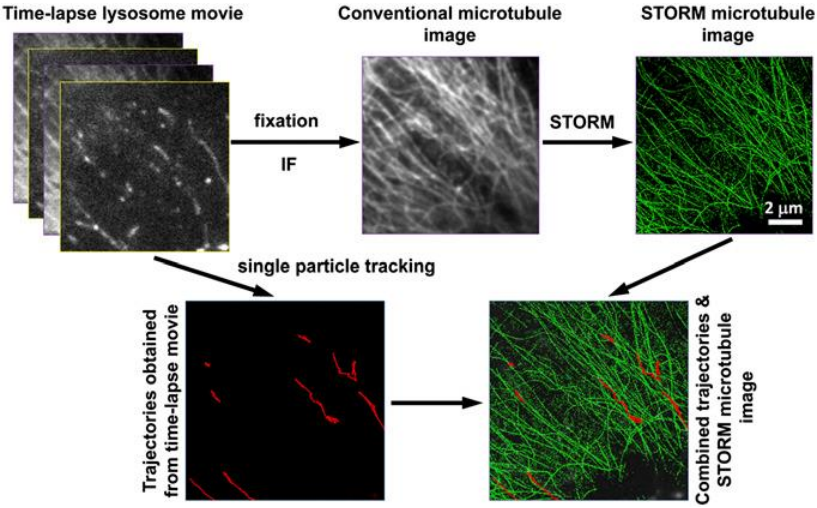

Figure 1.9 Lysosome trajectories extraction from time-lapse movie using SPT, and STORM imaging of microtubule network. *A live-cell time-lapse movie is recorded at high temporal resolution. The sample is then fixed and STORM imaging of the microtubule network is then recorded. Single-particle tracking is used to obtain trajectories from the live-cell movie, and these trajectories are precisely aligned with the STORM image of the microtubules using fiduciary markers. Image reprinted from ref.* [26]

Although SPT provides an extremely high and detailed amount of information on the system, however, extraction and processing of single trajectories renders this technique an inherently time-consuming approach. In addition, the application of this method usually does not render the structural information (size of the organelle) straightforward to retrieve.

1.5 Fluctuation-based techniques

1.5.1 Fluorescence Correlation Spectroscopy (FCS)

Fluorescence Correlation Spectroscopy (FCS) is a powerful tool to measure important physical quantities such as concentrations, diffusion coefficients, diffusion modes or binding parameters in living cells. Spatiotemporal correlation spectroscopy (FCS) techniques rely on temporal autocorrelation analysis of fluorescence intensity fluctuations collected in time from a tiny focal volume defined by the microscope focus of the excitation laser beam within a sample [46], its spatial resolution is limited by diffraction. The magnitude and time decay of the fluorescence intensity fluctuations contain information on the concentration and dynamics of the fluorescent molecules in the

observation volume. The principle of single-point FCS is illustrated in **Figure 1.10**.

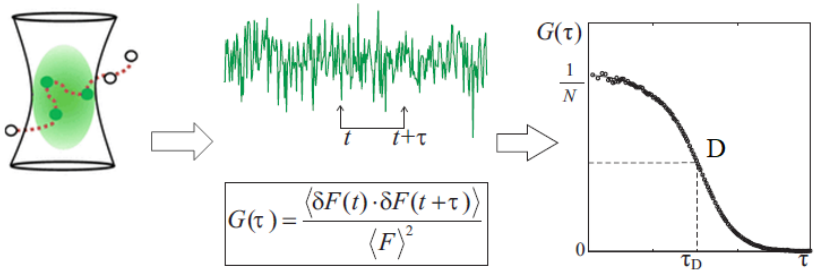

Figure 1.10 Principle of single-point FCS. *The PSF of laser is focused on a diffraction-limited point in the sample volume (left); fluorescent molecules (green dots) diffuse in the volume of the samples, entering and leaving the volume of the PSF. The fluorescent emission generated inside the PSF is collected and converted into an electric signal (centre); autocorrelation function is then computed using the equation shown in the middle where G(τ) represents the autocorrelation, τ the time lag, t the actual time of the electric signal and F(t) the electric signal originated from the fluorescence emission. Once the autocorrelation function is obtained (right) it is fitted to obtain the average number of particles inside the observation volume or the PSF (inversely proportional to G(0)) and the average diffusion coefficient D of the molecules that passed through the PSF during the acquisition time. Image adapted from ref.* [47]

1.5.2 Extending FCS to the spatial dimension: scanning-FCS and Raster Image Correlation Spectroscopy (RICS)

Although confocal FCS has lately become a more frequently applied technique to study the dynamics of membrane-bound fluorophores in

vitro, as well as in vivo [48–51], several limitations affect the accuracy of the measurements. The slow diffusion leads to long dwell times and, therefore, to longer measurements and strong photobleaching. During the measurement, the relative position of the detection volume with respect to the membrane has to be stable with an accuracy of about 100 nm [47]. Finally, measurements on biological membranes are particularly critical, since even tiny membrane movements or instabilities lead to severe artifacts [52]. To overcome these limitations, modifications of standard FCS have been developed [53–55], one of the most successful being scanning-FCS (sFCS) [56]. In sFCS the fluorescence is recorded from a small measurement volume defined by the focused illuminating beam as in FCS, and this measurement volume is moved relative to the sample in a controlled way [57]. Because the movement of the measurement volume in the sample is the only principal difference from FCS, all other features of FCS are preserved in sFCS, most importantly the high temporal resolution. This implementation has several advantages: sampling of a larger volume increases the statistical accuracy for slowly moving molecules and leads to shorter measurement times; short residence times in the detection volume reduce the effect of photobleaching; and the scan speed can be determined with high accuracy, eliminating the need for calibrating the detection volume [52]. The application of sFCS is

especially useful in measurements where diffusion is usually very slow such as on biological membranes.

As previously mentioned, another important development of single-point FCS is the so called “raster image correlation spectroscopy” (RICS) technique [54,58–60]. RICS exploits the optical sectioning of the PSF during a confocal microscopy acquisition. As depicted in **Figure 1.11**, in RICS, a spatial autocorrelation between adjacent pixels is performed [59].

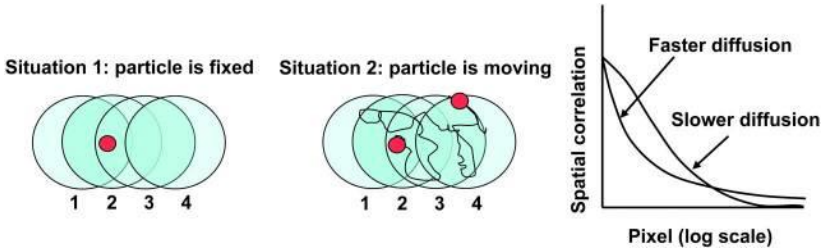

Figure 1.11 RICS principle. *Schematic representation of a raster scan acquisition of a confocal microscope and its spatial correlation analysis. (Situation 1, left) If a particle is fixed or slowly moving, its signal will be detected in position 1, 2 and 3 but not in 4 during a line acquisition. The spatial autocorrelation will show a slower motion of the particle (right, slower diffusion). (Situation 2, center) if a particle is moving quickly, there is a higher probability that it will be detected also in position 4 and this will then be visualized on the autocorrelation function (left, faster diffusion). The spatial autocorrelation function decays with a characteristic length that depends on the diffusion constant and the size of the illumination volume (PSF). Image reprinted from ref.*[59]

1.5.3 Phasor analysis of Local Image Correlation Spectroscopy (PLICS): recovering spatial information at the sub-cellular scale

Worthy of note, none of the extensions of FCS to the spatial dimension discussed above have clear potential to extract information on the structural properties (e.g. size, shape, etc.) of subcellular, dynamic nanosystems, although the spatial dimension is probed. To fill this gap, phasor analysis of local image correlation spectroscopy (PLICS) data was implemented as a new method by L. Lanzanò and co-workers [21]. PLICS exploits the pixel-by-pixel analysis of local spatial correlation functions and extracts relevant structural parameters of the diffusing object which are encrypted in the image stack [21]. The principle of PLICS technique is largely similar to those of FCS, with the remarkable difference that FCS is the analysis of intensity fluctuations in time, whereas image correlation spectroscopy is the analysis of intensity fluctuations in space [21]. The phasor analysis is used here conveniently as an unbiased, fit-free tool to characterize a large number of correlation functions. The PLICS algorithm is capable of mapping the sizes of elements contained in a heterogeneous system and provides the size and number of separate subspecies, which otherwise would be hidden in the average properties of a single

correlation function. PLICS has been applied in order to quantify the spatial and temporal heterogeneity in the size and number of intracellular vesicles in live cells [21]. As a paradox, however, in PLICS it is the temporal information that is lost.

1.5.4 Joining spatial and temporal information: Spatiotemporal Image Correlation Spectroscopy (STICS) and image-derived Mean Square Displacement (*i*MSD)

A complete analysis of the full space–time correlation function was proposed by Hebert *et al.* introducing the Spatiotemporal Image Correlation Spectroscopy (STICS) method [61]. STICS is based on a complete calculation of both the temporal and all-spatial correlation for intensity fluctuations from pixels separated by different frame of laser-scanning microscopy image series. This approach allows measurement of diffusion coefficients and mean molecular displacements down to a few tens of nanometers [62]. Since its introduction, however, the STICS approach has been mainly used exploring the second time range with frame rates. This in turn allowed accurate measurement of only slow protein fluxes (i.e., magnitudes of μm/min). In order to overcome this limitations, recently our group

proposed image-derived MSD (*i*MSD) as modified spatiotemporal image correlation spectroscopy approach, suitable for determining diffusion laws of GFP-tagged integral membrane proteins in live cells with high temporal and spatial resolution [15]. Di Rienzo and coworkers applied *i*MSD approach to study the regulation of protein diffusion taking place in the micro-to-millisecond time range on micrometer-sized membrane regions in live cells. By using a GFP-tagged variant of the TfR, they probed the regulation of protein diffusion imparted by the cytoskeleton meshwork (**Figure 1.12**) [15]. Notably, they obtain values for diffusion coefficient, confinement area, and confinement strength (and their dependence on specific drugs) that agree with those calculated for the same molecule in high-speed SPT measurements [63,64]. It is noteworthy that, unlike SPT, this correlation-based method works well with high molecular densities, low signal-to-background ratios, and high counting-noise levels. This combination of properties opens the way to "single-molecule" experiments with GFP-tagged proteins in the presence of many labeled molecules diffusing at the same time and within the PSF.

The *i*MSD approach can successfully recover diffusion constants, confinement area, and confinement strength coefficients over many micrometers on the membrane plane, and their variation in response

to drug treatments or temperature shifts. Moreover, *i*MSD method does not need any preliminarily assumption/knowledge on the system under study and, more importantly, does not need to extract the single trajectories.

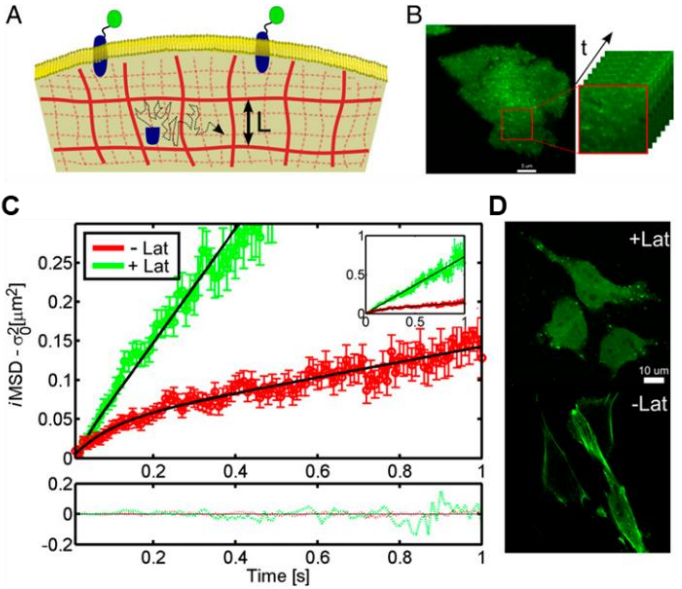

Figure 1.12 Analysis of TfR dynamics in living cells. *(**A**) Schematic representation of a GFP-tagged TfR diffusing in the cytoskeleton hierarchical meshwork, with particular emphasis on the spatial size accessible in the tens of milliseconds timescale. (**B**) Total internal reflection fluorescence microscopy image of a CHO cell expressing GFP-tagged TfR (Left) and the detail of the membrane patch used for the measurement (Right). (**C**) iMSD vs. time plot for GFP-TfR in physiological conditions (red curve) and after 30 min of Lat-B treatment (green curve). (Inset) iMSD trend at a short timescale. (**D**) Fluorescence images of cells transfected with actin- GFP, showing the effect of Lat-B on the integrity of actin filaments. Image adapted from ref.* [15]

In spite of the recent advances in live-cell imaging technologies (e.g. development of organelle-specific markers, optimization of labeling procedures, and availability of highly sensitive optical microscopes [65–67]), observing subcellular structures at high spatial and temporal resolution, and in living cells, is still a challenging task. By bringing the *i*MSD approach from the molecular to the subcellular scale, this work demonstrates that retrieving both structural and dynamic information of the cellular organelles is possible and can be achieved by a fast and robust procedure.

CHAPTER 2

2. *i*MSD: from molecular to sub-cellular scale

In this Chapter, image mean square displacement (iMSD) method is applied to the subcellular organelles to study their structural and dynamic properties. A unique triplet of average parameters (diffusivity, anomalous coefficient and size), extracted from each iMSD and represented in a 3D parametric space, define the so called "dynamic fingerprint".

Most of the content of this Chapter was peer-reviewed and published with co-authors in:

- *Digiacomo, L., D'Autilia, F., Durso, W., Tentori, P. M., Caracciolo, G., & Cardarelli, F. (2017). Dynamic fingerprinting of sub-cellular nanostructures by image mean square displacement analysis. Scientific reports, 7(1), 1-10.*
- *Ferri, G., Digiacomo, L., D'Autilia, F., Durso, W., Caracciolo, G., & Cardarelli, F. (2018). Time-lapse confocal imaging datasets to assess structural and dynamic properties of subcellular nanostructures. Scientific data, 5(1), 1-8.*

2.1 Image-derived MSD (*i*MSD) analysis on molecular scale

The typical scheme of an *i*MSD experiment is illustrated in **Figure 2.1**. The starting point is fast imaging of a given region of interest

within the cell. Then, the spatiotemporal correlation function is calculated comparing acquired images at increasing time delays, for example each 2, 3, n repetitions.

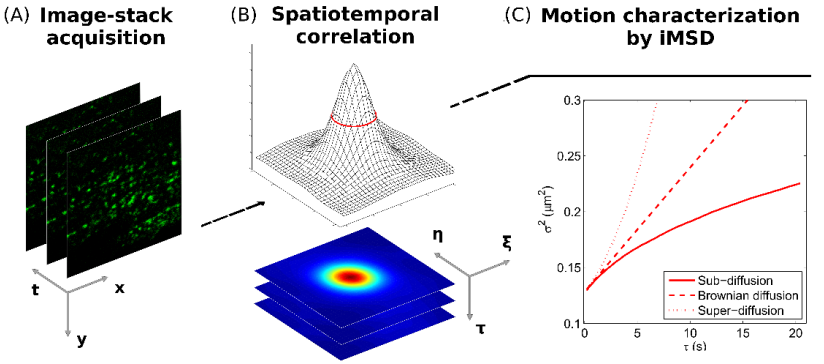

Figure 2.1 Schematic representation of the iMSD-based dynamic fingerprint analysis. *(**A**) A stack of images of fluorescently-labelled intracellular nano-structures is acquired by time-lapse confocal microscopy. (**B**) Spatiotemporal correlation function is derived from image analysis by the iMSD algorithm (see **Image processing and data analysis** for equations). (**C**) Gaussian fitting of correlation functions allows to extract the iMSD plot, which in turn depicts the average diffusion law of the structure of interest (exemplary cases are reported: super-diffusion, dotted red line; isotropic diffusion, dashed red line; sub-diffusion, solid red line).*

The width of the peak of the spatial autocorrelation function increases at increasing time delays as a function of the movement of the object of interest, independently of its particular mode of motion. By fitting the spatiotemporal correlation function, the average *i*MSD can be extracted. Three main *i*MSD results might be expected, that is: isotropic diffusion (dashed red line), super-diffusion (dotted red line),

or sub-diffusion/confined motion (solid red line). Thus, through fitting procedures of the spatiotemporal correlation function, we determined the kind of motion and measured all the relevant dynamic parameters. Among them, we especially focused on anomalous diffusion exponent α, short-term diffusion coefficient D_m and intercept value σ_0^2. This parameter can provide quantitative information about the size of the particle under study. To demonstrate this property, Di Rienzo *et al* performed a set of simulations in which particles of increasing sizes (R) freely diffuse in a box [15]. As shown in **Figure 2.2A**, changing the particle size does not affect the iMSD overall shape, but impacts on the intercept value. As expected, σ_0^2 increases for increasing R values. The difference between σ_0^2 and the independently measured PSF value (in the present example 300 nm) yields the actual particle size.

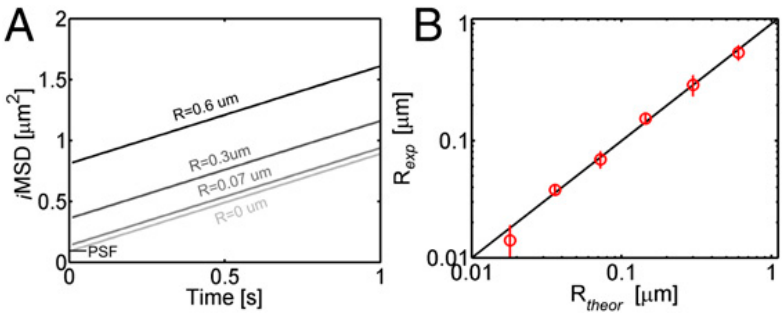

Figure 2.2 Effect of particle size on σ_0^2. *(**A**) iMSD is linear with increasing σ_0^2 values for increasing particle sizes. PSF on ordinate indicates the contribution of the instrumental waist to σ_0 value. (**B**) Accordance between the theoretical R value*

(imposed in the simulation) and that recovered from the analysis. Image reprinted from ref. [15]

Figure 2.2B shows the recovery of particle size in a rather broad range spanning from a few tens to several hundred nanometers.

2.2 Image processing and data analysis

Both the *i*MSD processing of the acquired image-stacks and the subsequent data analysis were carried out with custom scripts working on MATLAB (MathWorks Inc., Natick, MA). In detail, we firstly computed by Fourier methods the spatiotemporal correlation function of the fluorescence intensity fluctuations g, which is defined as follows:

$$g(\xi,\eta,\tau) = \frac{\langle i(x,y,t)\cdot i(x+\xi,y+\eta,t+\tau)\rangle}{\langle i(x,y,t)\rangle^2} - 1 \quad \text{(Eq. 1)}$$

where ξ and η are the distance between correlated pixels in the x and y directions, respectively, τ is the time lag, i(x, y, t) is the fluorescence intensity at point (x, y) and time t, and ⟨...⟩ indicates the average over spatial and time variables x, y and t [15]. g(ξ, η, τ) fit to standard Gaussian functions, i.e.

$$g(\xi,\eta,\tau) = g_0 + g_1(\tau)\exp\left\{-\frac{(\xi-v_\xi\tau)^2+(\eta-v_\eta\tau)^2}{\sigma^2(\tau)}\right\} \quad \text{(Eq. 2)}$$

where the numerator of the exponential term describes the net flux of particles along a specific direction in terms of average velocity, i.e. $\langle \vec{v} \rangle = \vec{v}_{\varphi} = (v_{\xi}, v_{\eta})$ and the variance $\sigma^2(\tau)$ represents the mean square displacement of the ensemble as a function of the time lag. Thus, overall information about the intracellular dynamics has been obtained by the analysis of $g(\xi, \eta, \tau)$, without extracting and processing single particle tracks. As an instance, we carried out a straightforward categorization of motion by fitting σ^2 to a power-law equation, i.e.

$$\sigma^2(\tau) = \sigma_0^2 + \kappa\, \tau^{\alpha} \quad \text{(Eq. 3)}$$

Where σ_0^2 is an intercept value related to the average particle size and the waist of the point spread functions [15,16] and α discriminates the dynamics as i) Brownian diffusion ($\alpha=1$), ii) super-diffusive motion ($\alpha>1$) and iii) sub-diffusion ($\alpha<1$). Furthermore, more accurate models allowed us to measure the involved dynamic parameters. More precisely, an anomalous diffusion with $\alpha < 1$ can be regarded as a confined motion and the trend of $\sigma^2(\tau)$ can be fitted to the following relationship [15]:

$$\sigma^2(\tau) = \sigma_0^2 + 4D_M\tau + \frac{L^2}{3}\left(1 - \exp\left\{-\frac{\tau}{\tau_c}\right\}\right) \quad \text{(Eq. 4)}$$

Where L defines the linear size of the confinement area, τ_c is an index of how fast confinement occurs, D_M is the particle diffusivity at large time scale and represents 1/4 of the derivative of σ^2 for $\tau \to \infty$. Similarly, the short-term diffusivity D_m is measured by the slope of σ^2 for $\tau \to 0$ and reads $D_m = D_M + L^2/(12\tau_c)$ [15]. On the other side, if $\alpha > 1$, the trend of $\sigma^2(\tau)$ is ascribable to the sum of a linear contribution due to Brownian diffusion and a parabolic term that describes a component of active transport along different directions on the focal plane [17]. In other words:

$$\sigma^2(\tau) = \sigma_0^2 + 4D\tau + v_\sigma^2\tau^2 \quad \text{(Eq. 5)}$$

Where v_σ^2 represent the variance of particle velocity (i.e. $v_\sigma^2 = \langle(\vec{v} - \langle\vec{v}\rangle)^2\rangle$) and D is the diffusion coefficient (which is the same both for short and long time scale). Therefore, we characterized the intracellular dynamics through Eq. 3-5. Finally, we point out the possibility to describe more complex dynamics as, for instance, that of structures undergoing super-diffusive motion at a short time scale and confined diffusion at a larger time scale. To describe these systems, we propose the following generalization of the aforementioned models:

$$\sigma^2(\tau) = \sigma_0^2 + 4D_M\tau + \frac{L^2}{3}\left(1 - \ e\exp\left\{-\frac{\tau}{\tau_c}\right\}\right) + v_\sigma^2\tau^2 \ e\exp\left\{-\frac{\tau}{\tau_v}\right\}$$

(Eq. 6)

Where τ_v ($\tau_v < \tau_c$) represents a characteristic time, below which the super-diffusive trend is dominant. Since the parabolic contribution decreases exponentially, at larger time delays it becomes negligible and the *i*MSD trend is determined by the confinement term. Worthy of note, this "global" model describes hybrid super/sub-diffusive behaviors within the employed correlation time window and preserves the physical meaning and the corresponding derivation of all the parameters, which are included in the previous descriptions. Finally, those models are included in Eq. 6 as particular cases, i.e. Eq. 4 and Eq. 5 can be regarded as limits of Eq. 6 for $\tau_v \to 0$ and $\tau_v \to \infty$, respectively.

2.3 *i*MSD analysis: from molecules to sub-cellular nanostructures

At the subcellular scale, as mentioned earlier, the average size of the diffusing objects becomes typically comparable with the characteristic size of the observation spot and, as a consequence, measurable. Thus,

at this scale, the parameters of a time-lapse imaging acquisition suitable for proper *i*MSD analysis can be adjusted based on the known characteristic size of the object of interest. We proved this basic principle by exploiting the lysosome as target organelle. (**Figure 2.3**). We can assume that only if the time resolution of imaging is appropriate to describe the motion of the organelle under study, this latter will appear as 'immobile' within each captured frame, i.e. it will display a characteristic size that, on average, is not deformed due to the imaging speed. We can also reason to artificially immobilize the organelle of interest by fixing the sample. This condition can be used as a reference to obtain the expected organelle size under the imaging conditions chosen (e.g. laser wavelength, pixel size, objective, etc.). This is shown in **Figure 2.3A-C** for lysosomes, along with an acquisition performed in live cells at the desired temporal resolution (i.e. 65 ms/frame, **Figure 2.3B**), and an acquisition performed intentionally at slow speed (i.e. 10 sec/frame, **Figure 2.3C**). Thus, we show quantification of organelles sizes directly from the optical microscopy images (**Figure 2.3D**).

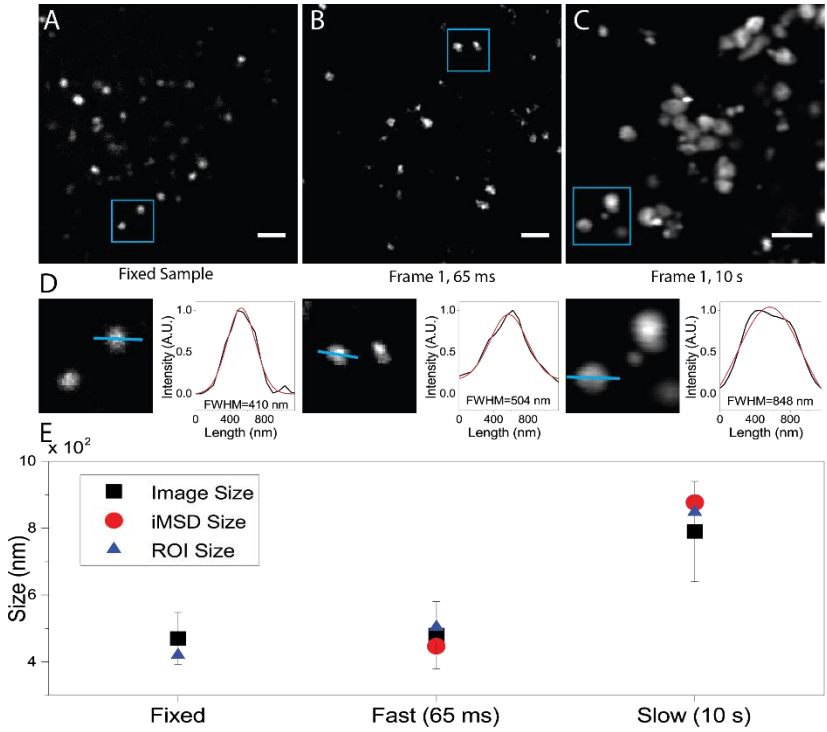

Figure 2.3 Setting the experimental parameters. *(**A**) Exemplary image of stained lysosomes in a fixed sample. Scale bar: 2 μm (**B**) First frame of a stack of images of stained lysosomes in a living cell, acquired with the appropriate parameters. Temporal resolution: 65 ms/frame. Scale bar: 2 μm (**C**) First frame of a stack of images of stained lysosomes in a living cell, acquired at low speed: artifactual deformation of the apparent lysosome size due to organelle motion during imaging is clearly visible. Temporal resolution: 10 s/frame. Scale bar: 2 μm. (**D**) Example of size calculation for imaged lysosomes in blue ROI of (A), (B) and (C). The intensity profile along the blue line was fitted with a Gaussian function to retrieve the FWHM, i.e. an estimate of spot size. FWHM values are reported for each fitting. (**E**) Graphical representation of size values obtained by image analysis described in panel (**D**) for all imaged lysosomes (black square, mean value and standard deviation), for*

lysosomes enclosed within the blue ROI (blue triangle) and retrieved by iMSD analysis (red circle).

In particular, the size of each organelle/structure in the image is extracted by means of ImageJ software. For each spot of imaged lysosomes, intensity profile is plotted and fitted with a Gaussian function to obtain full width at half maximum (FWHM) value that can be assumed as estimation of spot diameter. As expected (**Figure 2.3** e), the acquisition performed at an appropriate temporal resolution (65 ms, in this case) yields a characteristic size of the structure of interest that closely resembles that obtained from the fixed sample, either by using the standard tool described above or the *i*MSD y-axis intercept. By contrast, the artificially slow acquisition yields a substantially enlarged apparent size of the same structure, due to its substantial movement during imaging. It is clear that, under these latter experimental conditions, both the structural and dynamic information embedded into the time-lapse acquisition do not faithfully describe the intrinsic properties of the structure of interest. Concerning the spatial dimension, it is suggested to oversample the pixel by the available PSF of the laser beam, i.e. set a pixel size at least 3–5 times smaller than the PSF.

2.4 The role of the time window: super-diffusive or sub-diffusive lysosomes?

A fully expected property of the proposed analysis is that the overall shape of the resulting *i*MSD must strictly depend on the timescale considered. A limit case on a very large timescale, for instance, is the total confinement due to the plasma membrane impenetrable boundary, irrespective of the chosen intracellular structure. On the other end, on a very short timescale, one may expect to grab the local mode of motion of the structure. To show how this applies to a real case, we show here an application to the lysosome.

Lysosomes are sub-micrometric, dynamic, membrane-enclosed sub-cellular organelles. They represent the main degradative compartments of the cell [68], but have recently been proposed as signaling hubs, with a central role in a number of crucial processes, from nutrient sensing to metabolism and cell growth regulation [69,70]. As for many other sub-cellular structures/compartments, it is now well appreciated that the simultaneous tight control of lysosome structural (e.g. size) and dynamic (e.g. diffusivity, mode of motion) properties is key to their function in the cell, in physiology and in pathology [19,71–73]. In spite of the huge research efforts, retrieving quantitative,

simultaneous access to both structural and dynamic information on such tiny subcellular structures remains a challenge in the field.

Technically, we performed three consecutive measurements on the same cell, at three different timescales, namely: *i*) a short timescale (0-0.5 seconds), *ii*) an intermediate timescale, coincident with that used for all the structures (0-12 seconds), and *iii*) a long timescale (0-60 seconds) (**Figure 2.4**). At first glance, the *i*MSD analysis reveals three very different dynamic fingerprints of the lysosome. In particular, on the shortest timescale, the *i*MSD plot clearly shows the emergence of an average super-diffusive behavior of lysosomes (α=1.24±0.13) (Fig. 3).

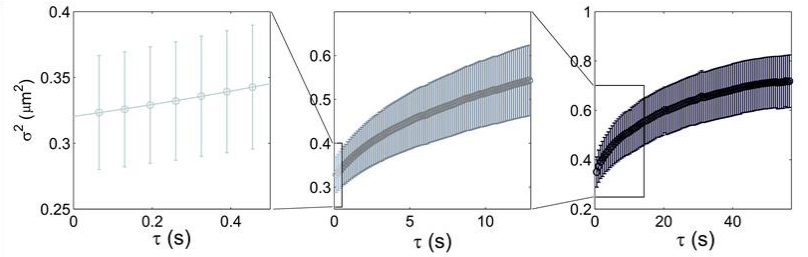

Figure 2.4 Exemplary iMSD plots of the lysosome at three different temporal scales*: short, 0-0.5 seconds (left, light grey); intermediate, 0-12 seconds (middle, grey); long, 0-60 seconds (right, dark grey).*

Please consider that this corresponds to active transport of lysosomes along different (random) directions (with a measured speed of about 0.12 μm/s), as no overall movement of the peak of the spatiotemporal correlation function (i.e. concerted movement of the lysosomes in one preferential direction) was detected. Of note, this result speaks in favor of lysosome possible movement along cytoskeleton components (possibly microtubules, based on previous evidences [74,75]). As a control for this, we performed an experiment in presence of 10 μM Nocodazole (see **Materials and Methods** for more details) to induce selective microtubule depolimerization. As expected, under these conditions, lysosome super-diffusive behavior vanishes in favor of a slightly sub-diffusive local motion ($\alpha=0.81 \pm 0.33$) and a sensibly reduced local diffusivity ($D_m=[3.3 \pm 1.6]x10^{-3}$ $\mu m^2/s$) (**Table 3.1**). Of note, the super-diffusive behavior vanishes also if we extend the timescale of the acquisition. At an intermediate timescale (the same reported in **Figure 2.9**) the average dynamics of lysosomes is characterized by α coefficient below 1, indication of a sub-diffusive behavior that can be readily ascribed to the effect of the complex intracellular environment on lysosome movement. This effect is much more evident if the timescale of the acquisition is further extended to 60 seconds ($\alpha=0.33 \pm 0.10$) (**Figure 2.5** and **Table 2.1**).

The detected super-diffusive and sub-diffusive trends at different timescales can be described by a unique model, which quantifies the time extent within which the super-diffusion is dominant, as well as all the other involved dynamic parameters.

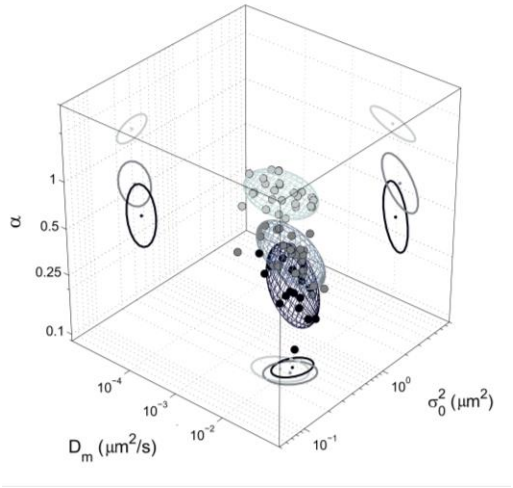

Figure 2.5 Dynamic fingerprint of the lysosome at different spatiotemporal scales. *3D plot of the dynamic fingerprint of the lysosome at the three different temporal scales.*

This description is expressed by Eq. 6 and overcomes the apparent incoherence of the measured α-values associated to the same sub-cellular structure. In this regard, **Figure 2.6** shows a representative

experimental curve and the corresponding fitting curve (red) that has been computed according to Eq. 6.

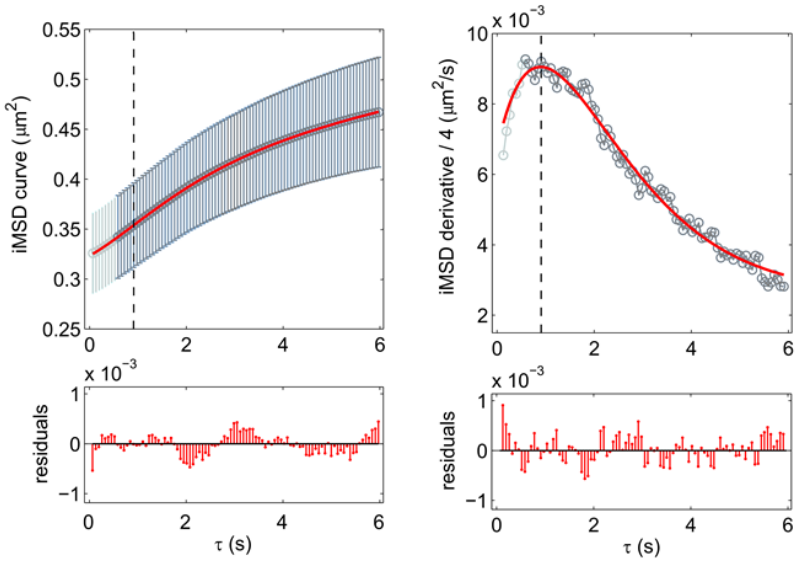

Figure 2.6 The first 6 seconds of the iMSD plot of Figure 2.4. *The graph (left panel) shows the goodness of the fit to the global model (red line and residuals, Eq. 6 in* ***Image processing and data analysis****). The derivative of the iMSD plot shows the trend of the measured diffusivity right panel).*

The model is in good agreement with the experimental trend and the transition from super- to sub-diffusion is even more noticeable in the derivative plot, which shows an almost linear increase in the particle mobility at short timescale (super-diffusion) from an intercept value

D_m, until a maximum is reached and then an exponential fall (sub-diffusion) toward an asymptotic value D_M.

In conclusion, we show that lysosome mobility is a combination of active transport and sub-diffusion. By averaging the behavior of many lysosomes at the same time, we can define directed motion and sub-diffusion as 'collective' transport properties for this organelle within the cytoplasm. It is worth noting that these two modes of motion were already proposed based on tracking experiments conducted on single, isolated lysosomes [14,76]. What we can add here by *i*MSD analysis is the average spatiotemporal relationship between these two processes: active transport regulates lysosome movement, on the average, at a short timescale (and small spatial scale), while sub-diffusion plays a major role, on the average, at a longer timescale (and larger spatial scale). In this regard, interestingly, Balint et al. recently proposed a model of lysosome motion postulating that the intersections between microtubules are able to impose a significant hindrance to directed motion, thus leading to long pauses in transport or, eventually, switches to diffusion [26] (**Figure 2.7**). Our results, in keeping with such model, define the average spatial (and temporal) extent of the contribution of directed motion along microtubules.

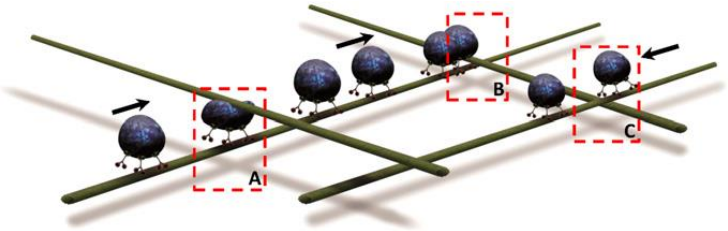

Figure 2.7 Mechanistic model of lysosome transport along microtubule network. *When cargo arrives at a microtubule–microtubule intersection in which the axial separation of the intersecting microtubules is larger than 100 nm, there is minimal hindrance to the forward motion and transport continues on the same microtubule without disruption (**A**). When the axial separation of the intersecting microtubules is less than 100 nm, the intersection presents a major obstacle, stalling the motors and momentarily stopping forward motion until the obstacle is overcome (**B**). Cargos that are not positioned between the intersecting microtubules continue moving forward on the same microtubule without feeling the obstruction from the intersection (**C**). Image reprinted from ref.* [26]

2.5 The dynamic fingerprint of intracellular structures

At this point, having set the basic rules for *i*MSD calibration, the approach is ready to be used in a number of different applications at the subcellular scale. To prove this potency, variants of the major structures involved in endocytic processes (namely: caveolae, clathrin-coated vesicles, and macropinosomes) and in the subsequent intracellular processing of internalized cargoes (namely: early endosomes, late endosomes, and lysosomes) were fluorescently

labelled. For each of these structures, the local diffusivity (D_{micro}, hereafter D_m), the anomalous-diffusion coefficient (α), and the offset parameter (σ_0^2) are extracted by fitting the *i*MSD plot and represented in a parametric 3D space, within which the results of a specific image-stack correspond uniquely to a data point. In turn, a set of image-stacks exploring the dynamics of a specific sub-cellular structure defines a multivariate 3D distribution, with particular location and orientation in the parameter-space. We quantified these geometrical features by diagonalizing the covariance matrix of the distribution, then we defined the resulting ellipsoid according to the obtained eigenvalues and eigenvectors. In this way, the space within the ellipsoidal surface can be regarded as the analogue of the confidence interval [mean - SD, mean + SD] for 1-dimensional distributions. In this way, the whole population of diffusing objects probed for each cell will be represented by a unique triplet of parameters, i.e. by a single point in the 3D plot. Thus, clustering of single-cell experimental points readily depicts what we call the "dynamic fingerprint" of the selected structure at the whole-cell-population level. Worthy of note, by this approach we easily demonstrate that each of the analyzed structures segregates into a separate region of the chosen parametric space, according to the almost unique combination of its characteristic average size and dynamic properties.

Figure 2.8A and **B** show live-cell confocal images and representative *i*MSD traces of three well known subcellular structures involved in endocytic processes in HeLa cells, namely caveolae (red curve), clathrin-coated vesicles (blue curve) and early macropinosomes (green curve). The definition 'early' is here used to distinguish measurements performed on macropinosomes at early stages of trafficking (i.e. within 80 minutes after administration) from those performed at an intermediate stage (i.e. from 80 to 120 minutes after administration) and from those performed at late stages (i.e. after more than 120 minutes from administration).

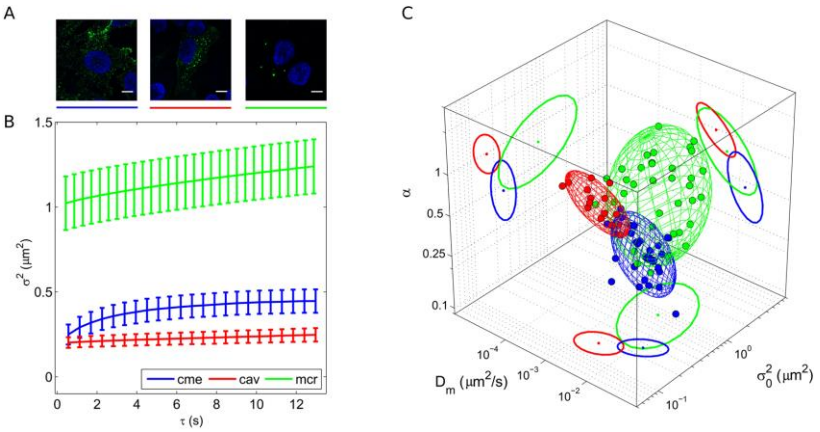

Figure 2.8 Dynamic fingerprint of exemplary intracellular nanostructures. ***(A)*** *Representative confocal images of clathrin-coated vesicles, macropinosomes, and caveolae, respectively (green signals). The blue signal indicates the nucleus. Scale bar: 10 μm.* ***(B)*** *Representative iMSD plots of the three structures with error bars*

*(clathrin-coated vesicles in blue, macropinosomes in green, and caveolae in red). (**C**) 3D plot of extracted parameters shows the differences in the dynamic (short-range diffusivity and anomalous coefficient) and structural (size) properties of the selected structures.*

These latter cases are discussed later in the text and presented in **Figure 2.10**. The *i*MSD traces, already by visual inspection, reveal clear differences in the characteristic structural and dynamic properties of the selected structures. More quantitatively, the extracted parameters (D_m, α, and σ_0^2) are combined together, as described above, to highlight the characteristic dynamic fingerprint of each structure (**Figure 2.8C**). A few aspects are worthy of mention. First, the three pathways are clearly distinguishable one from the other in terms of the average characteristic size of the structures involved. Although we cannot directly compare our data with previous electron-microscopy-based analyses on these organelles (e.g. [77–79]), the retrieved σ_0^2 values nicely match the expectations, with macropinosomes being, on the average, larger than clathrin-coated vesicles and caveolae (**Figure 2.8C**, see also **Table 2.1**). In addition, from a dynamic point of view, clathrin-mediated endocytosis appears to involve structures substantially more mobile, in terms of local diffusivity (D_m=[16.2 ± 9.9]x10^{-3} $\mu m^2/s$), as compared to both caveolae ([3.1 ± 1.8]x10^{-3} $\mu m^2/s$) and macropinosomes ([8.3 ± 9.0]x10^{-3} $\mu m^2/s$). This result is not surprising, as clathrin-coated vesicles are known to readily detach

from the plasma membrane (in a few seconds [80]) to become free to move across the cytoplasm.

	α	**σ_0^2 (μm^2)**	**D_m (x10^{-3}μm^2/s)**	**D_M (x10^{-3} μm^2/s)**
cme (33)	0.48 ± 0.17	0.27 ± 0.06	16.2 ± 9.9	2.8 ± 1.3
cav (15)	1.00 ± 0.22	0.17 ± 0.04	3.1 ± 1.8	1.2 ± 0.5
***e*-mcr** (23)	0.79 ± 0.27	1.13 ± 0.95	8.3 ± 9.0	2.5 ± 2.2
***i*-mcr** (38)	0.60 ± 0.38	0.52 ± 0.28	13.7 ± 19.9	2.2 ± 2.7
***l*-mcr** (25)	0.39 ± 0.21	0.37 ± 0.16	5.8 ± 4.7	0.4 ± 0.3
***e*-endo** (41)	1.02 ± 0.20	0.16 ± 0.08	3.0 ± 2.4	1.1 ± 0.6
***l*-endo** (58)	0.58 ± 0.16	0.50 ± 0.15	15.4 ± 10.6	3.1 ± 1.8
lyso (60)	0.56 ± 0.12	0.29 ± 0.10	12.3 ± 7.0	2.7 ± 1.0
lyso_*fast* (26)	1.24 ± 0.13	0.32 ± 0.08	11.9 ± 7.3	10.4 ± 7.6
lyso_*medium* (26)	0.55 ± 0.13	0.33 ± 0.10	13.0 ± 6.7	2.6 ± 1.5
lyso_*slow* (26)	0.33 ± 0.10	0.39 ± 0.10	10.4 ± 3.7	1.2 ± 0.5
lyso *fast* + NCZ (7)	0.81 ± 0.33	0.39 ± 0.08	3.3 ± 1.6	1.6 ± 1.0

Table 2.1 Parameters extracted from the iMSD fitting. *Values are reported as Mean ± Standard Deviation. The number of cells analyzed for each sample is reported in the first column, within brackets.*

By contrast, caveolae are characterized by quite long residency times at the plasma membrane, and slow intracellular trafficking [81]. Similarly, macropinosomes at an early stage of formation are large, membrane-bound structures, whose detaching and subsequent trafficking necessitates coordinated cellular processes to be executed, such as actin polymerization, ruffle closure, etc. [82]. Interestingly,

however, the combination of such differences in local mobility of these structures with their respective average anomalous coefficient ($\alpha = 0.48 \pm 0.17$ for clathrin-mediated endocytosis, and $\alpha = 1.00 \pm 0.22$ and 0.79 ± 0.27 for caveolae and macropinosomes, respectively) produce the effect that they become quite similar if compared on the basis of their long-range diffusivity (D_M, see **Image processing and data analysis**; values are reported in **Table 2.1**), i.e. they are able to explore the intracellular environment to a very similar extent, at large spatial scales.

2.6 The dynamic fingerprint of the endosome-lysosome pathway

At this point, by means of *i*MSD we characterized the dynamic fingerprint of the entire 'endosomal-lysosomal system' [20], one of the main intracellular pathways devoted to the processing of internalized cargoes, that is: early endosomes, late endosomes and lysosomes (representative images of their fluorescently labelled variants and average *i*MSD curves are shown in **Figure 2.9A**).

The extracted parameters depict a scenario in which the transition from early to late endosomes entails the involvement of larger (shift

in σ_0^2, from 0.16 ± 0.08 μm^2 to 0.50 ± 0.15 μm^2) and more mobile (shift in local diffusivity, D_m, from [3.0 ± 2.4]x10^{-3} μm^2/s to [15.4 ± 10.6]x10^{-3} μm^2/s) structures (see **Figure 2.9B-C** and **Table 2.1**).

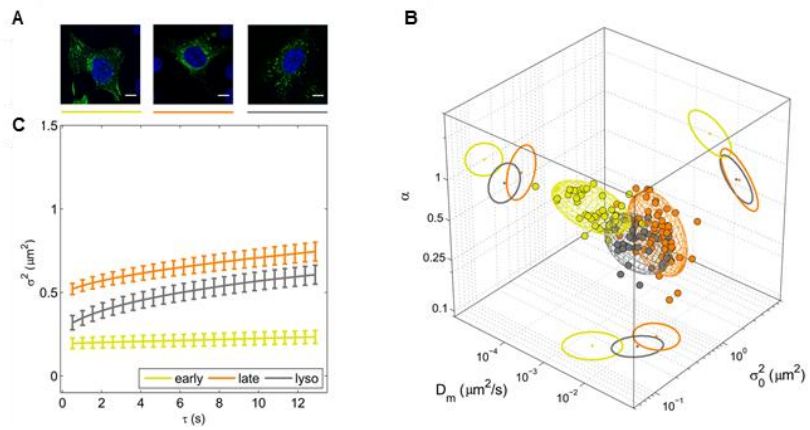

Figure 2.9 Dynamic fingerprint of the endosome-lysosome pathway. *(**A**) Representative confocal images of early endosomes, late endosomes, and lysosomes, respectively (green signals). Scale bar: 10 μm. (**B**) Representative iMSD plots of the three structures with error bars (early endosomes in dark yellow, late endosomes in orange, and lysosomes in grey). (**C**) 3D plot of extracted parameters shows the differences in the dynamic and structural properties of the selected structures.*

The increase in size is not surprising, as late endosomes are known to have the morphological characteristics of multivesicular bodies [83]. On the other hand, the increased diffusivity of late endosomes can be linked to their preferential localization in the center of cell cytoplasm, as compared to early endosomes, which are mainly membrane-located

organelles [84]. Also, the (apparent, as explained above) contradiction of the Stokes-Einstein relation at short spatial scales is compensated, at larger spatial scales, by the differential contribution of the anomalous coefficient α (1.02 ± 0.20 for early endosomes and 0.58 ± 0.16 for late endosomes), so that the long-range dynamic behavior of these structures is quite similar (D_M values in **Table 2.1**). Finally, transition from late endosomes to lysosomes entails an expected decrease of the characteristic average size of the structures, while no significant changes in local diffusivity are observed (**Table 2.1**).

2.7 The 'strange' case of the evolving macropinosome

It is worth spending a few words on the case of macropinosomes and the results obtained by *i*MSD on these subcellular targets. As mentioned above, macropinocytosis defines a series of events initiated by extensive plasma membrane reorganization or ruffling to form an external macropinocytic structure that is then enclosed and internalized [77]. Internalized macropinosomes at an early stage of trafficking share many features with phagosomes and both are distinguishable from other forms of endocytic vesicles by their large size (see results in **Figure 2.10**), morphological heterogeneity and lack

of coat structures. In general, the paucity of information available on macropinocytosis has hampered efforts to characterize its dynamics and to identify regulatory proteins that are expressed in order to allow it to proceed. What is known from biochemical analyses is that, after internalization, macropinosomes gradually get enriched of regulatory proteins common to other endocytic pathways, in turn suggesting that their identities as unique structures are short-lived [82]. In particular, by using antibodies against known markers of the endosomal pathway in fixed cells, it was shown that macropinosomes progressively develop classical endosomal characteristics before diminishing in size, developing into late endocytic structures (e.g. lysosomes) or eventually losing their identity via membrane retrieval [85,86]. To our knowledge, however, no report thus far addressed this endocytic route (and its temporal evolution) from a dynamic point of view in live cells. Here we address this process by the *i*MSD approach. After 20-min incubation of cells with 70-kDa dextrans, we acquired time series of trafficking macropinosomes at different time points, from 30 minutes up to approximately 3 hours after treatment. For simplicity, we divided the time points into three major groups: early macropinocytosis (30-70 min, already discussed, *e*-mcr in **Table 2.1**), intermediate macropinocytosis (80-120 min, *i*-mcr in **Table 2.1**), and late macropinocytosis (>120 min, *l*-mcr in **Table 2.1**). Nicely, we are able

to highlight the gradual change in the structural and dynamic properties of macropinosomes during trafficking (**Figure 2.10A**). While no significant changes in the local diffusivity of macropinosomes occurs during trafficking, both their size and overall mode of motion (α) are substantially modified in time (3D plot of **Figure 2.10A**).

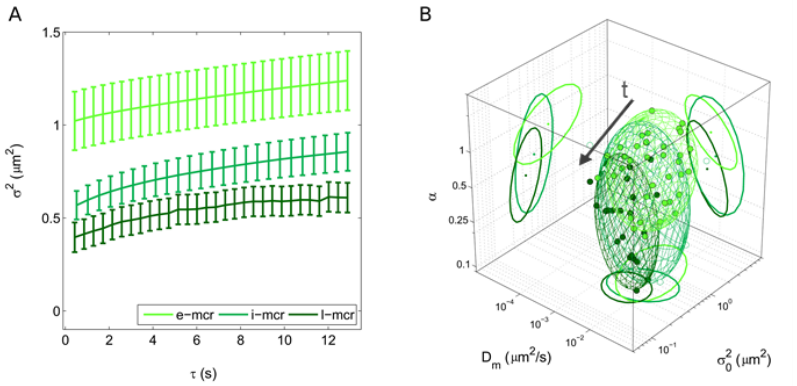

Figure 2.10 The time evolution of the macropinosome dynamic fingerprint. *(**A**) Exemplary iMSD plots of macropinosomes at three different stages of trafficking: early (30-70 min), intermediate (80-120 min), and late (>130 min). (**B**) 3D plot showing the time evolution of the dynamic fingerprint of macropinosomes from early (light green) to intermediate (white) and finally late (dark green) stages of trafficking.*

In particular, during trafficking, we observe a gradual decrease of the macropinosomes average size (**Figure 2.10A** and **B**, see also **Table 2.1**), and a concomitant increase of the sub-diffusive nature of their

motion (**Figure 2.3A** and, see also **Table 2.1**). As a further analysis, we calculated the number of macropinosomes in each acquisition: results are reported in **Figure 2.11B** and clearly show an increase of N in time.

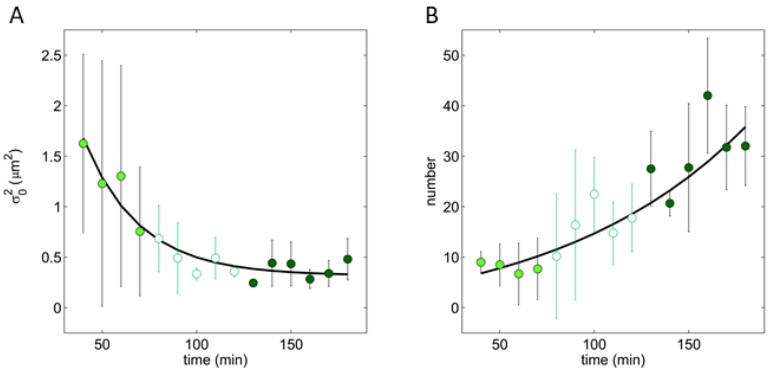

Figure 2.11 The time evolution of the macropinosome in size and number. ***(A)*** *Statistics on the average size (offset, σ^2) of macropinosomes observed at the different time points.* ***(B)*** *Statistics on the average number (N) of macropinosomes observed at the different time points.*

Overall, these observations well depict a scenario in which the macropinosomes originate as large structures at the membrane and then evolve, during intracellular trafficking, by decreasing in size and increasing in number. These results highlight the evolving 'dynamic nature' of these organelles that, together with their 'biochemical nature', defines their overall functional properties within the cell.

CHAPTER 3

3. Probing labeling-induced alteration of lysosome structural/dynamic properties by *i*MSD

In this Chapter, alterations of structural and dynamic properties of lysosome, caused by labelling strategies and/or procedures, are probed using iMSD. In particular, it is shone how Lipofectamine reagents, used to transiently express lysosome markers fused to fluorescent proteins, irreversibly alter the organelle structural identity. On the other hand, Effectene- and electroporation-based strategies are able to preserve lysosome structural and dynamic identity.

Most of the content of this Chapter was peer-reviewed and published with co-authors in:

- *Durso, W., D'Autilia, F., Amodeo, R., Marchetti, L., & Cardarelli, F. (2018). Probing labeling-induced lysosome alterations in living cells by imaging-derived mean squared displacement analysis. Biochemical and biophysical research communications, 503(4), 2704-2709.*

Our ability to study lysosome function in living cells strictly relies on the use of lysosome-specific fluorescent probes tailored to optical microscopy applications. An often neglected aspect is probing the influence of labelling strategies/procedures on lysosome properties in

live cells. In this Chapter the alterations of lysosome structural and dynamic properties upon labeling are investigated by means of *i*MSD.

3.1 *i*MSD detects structural and dynamic alterations of lysosome induced by labelling

We showed how the retrieved lysosome structural and dynamic features change depending on the experimental parameters (e.g. time scale selected, temporal resolution, pixel size, etc.), thus identifying specific guidelines for lysosome proper imaging and *i*MSD-based analysis [87,88]. Still, an unavoidable requirement for optical-microscopy-based analyses in living cells is labelling the structure of interest by fluorescent probes. This is typically achieved by either targeting a fluorescent (organic) dye to the lumen of the lysosome (e.g. LysoTracker) or by covalently attaching a genetically-encoded fluorescent protein (FP) to a lysosomal protein marker [89]. This latter is then expressed upon transient or stable transfection of the corresponding plasmid by means of standard procedures, such as lipofection or electroporation. In spite of the large amount of data produced in live cells on lysosomes following these procedures, little is known about the effect of standard labelling strategies on the

average structural and dynamic properties of this organelle. We tackle this issue here by the *i*MSD approach.

We benchmarked lysosome structural and dynamic features by using the standard fluorescent dye LysoTracker Red administered to HeLa cells following manufacturer's protocol. Time-lapse imaging of a region of interest ([17.28x17.28] µm) within the cell cytoplasm at a fixed total timescale (0-12 seconds) was performed (**Figure 3.1A**).

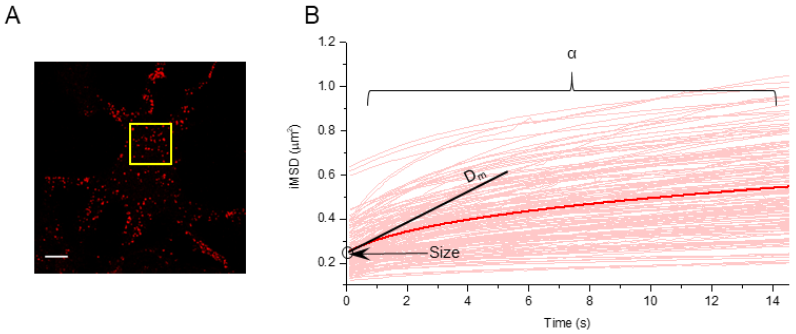

Figure 3.1 iMSD analysis to calculate the average structural and dynamic properties of lysosomes. *(**A**) Confocal fluorescence microscopy image of a control HeLa cell shows the normal distribution of lysosomes labeled with LysoTraker Red. A stack of images from a sub-region of the image (yellow square) is acquired with temporal resolution of 112 ms. Scale bar 10 µm. (**B**) Plot of iMSD vs. time of control lysosomes populations with the average trace in red and the three output parameters (size, D_m and α) indicated.*

Spatiotemporal correlation analysis is performed on the acquired image stacks to calculate the average displacement of lysosomes. The

whole population of retrieved *i*MSD traces is reported in **Figure 3.1B**, together with the average trace (bold red line). *i*MSD fitting yielded a quantitative picture of the average lysosome structural and dynamic properties in our experiments. In particular, the measured σ_0^2 (y-axis intercept of the *i*MSD trace, used to estimate the organelle size, as previously demonstrated [87]), D_m (local diffusivity), and α coefficient (anomalous diffusion coefficient) are reported, in the form of Mean ± SD values, in **Figure 3.2**, red squares (see also **Table 3.1**).

As expected, results are in line with our previous observations [87,88], and with available literature [90]. These benchmark values were further tested by probing expected variations of lysosome size and dynamics. Concerning size, cells were treated with 50 μM Sucrose and then imaged using Lysotracker. Since sucrose is not degraded within the lysosome, it is accumulated and induces an osmotic-swelling effect on the organelle [14]. In fact, *i*MSD analysis highlights an average increase (approximately 100 nm) in lysosome size upon Sucrose treatment (**Figure 3.2**, white squares and **Table 3.1**), with a concomitant minor effect on dynamics. Concerning dynamics, lysosome local diffusivity (D_m) was dramatically reduced upon ATP depletion (**Figure 3.2**, black squares and **Table 3.1**), with no effect on lysosome size.

	Construct	N	Size (µm)	Dm (µm^2/s)	α
Control		143	471 ± 66	0.015 ± 0.01	0.49 ± 0.13
Sucrose		176	641 ± 119	0.02 ± 0.009	0.34 ± 0.1
ATP depletion		78	469 ± 68	0.004 ± 0.003	0.55 ± 0.09
Lipofectamine	CD63 4h	59	658 ± 138	0.01 ± 0.006	0.53 ± 0.11
	CD63 24h	54	774 ± 137	0.017 ± 0.01	0.48 ± 0.16
	LAMP1 4h	46	602 ± 107	0.014 ± 0.007	0.48 ± 0.13
	LAMP1 24h	72	723 ± 137	0.018 ± 0.01	0.45 ± 0.14
	EGFP 4h	31	611 ± 90	0.01 ± 0.007	0.49 ± 0.09
	EGFP 24h	41	722 ± 141	0.013 ± 0.007	0.46 ± 0.12
Effectene	CD63 24h	48	675 ± 151	0.011 ± 0.007	0.45 ± 0.13
	LAMP1 24h	69	622 ± 193	0.012 ± 0.009	0.5 ± 0.13
	EGFP 24h	30	480 ± 157	0.007 ± 0.005	0.58 ± 0.24
Ctrl electroporation		25	422 ± 50	0.015 ± 0.007	0.53 ± 0.13
Electroporation	CD63	79	689 ± 201	0.012 ± 0.007	0.51 ± 0.13
	LAMP1	119	649 ± 157	0.017 ± 0.01	0.47 ± 0.12
	EGFP	14	507 ± 65	0.01 ± 0.008	0.52 ± 0.21
Baculovirus	LAMP1	45	728 ± 202	0.01 ± 0.009	0.51 ± 0.2
Stable transfection	CD63	44	526 ± 104	0.008 ± 0.004	0.49 ± 0.13
	LAMP1	44	502 ± 100	0.006 ± 0.003	0.5 ± 0.12
Ctrl stable transfect.		23	461 ± 79	0.006 ± 0.003	0.59 ± 0.1
Recovery 48h	EGFP 24h	28	676 ± 118	0.012 ± 0.006	0.53 ± 0.11

Table 3.1 Parameters extracted from the iMSD fitting. *Values are reported as Mean ± Standard Deviation.*

This matches previous results by Mithieux, G. & Rousset, B. [75], and is probably due to a more persistent interaction of lysosomes with microtubules in absence of ATP. We set out to study a number of lysosome-specific labeling strategies/procedures, which are routinely used worldwide. In particular, as mentioned above, we selected two specific protein markers of the lysosome, namely, LAMP1 and CD63 (**Figure 3.3**).

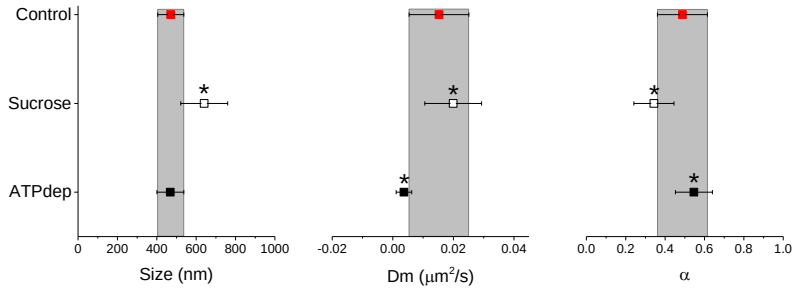

Figure 3.2 Variation of lysosome size and dynamics detected by iMSD. *Comparison between the average size, D_m and α values of the control (±SD) with those obtained under Sucrose exposure and ATP depletion. The '*' symbol indicates a Kolmogorov-Smirnov test with p≤0.001. The number of analyzed cells for each condition are reported in* ***Table 3.1****.*

Their FP-tagged variants were introduced into cells by transfection, either transient (using Lipofectamine, Effectene, or electroporation) or stable, in HeLa cells. As an obvious control, we probed that lipofection resulted in the proper co-localization of both CD63-EGFP and LAMP1-GFP with the LysoTracker fluorescence signal (**Figure 3.4**, using Lipofectamine), in keeping with previous reports [14,91–94]. All tested conditions were compared to the Lysotracker-based benchmark by statistical meta-analysis on the three measured parameters, σ_0^2, D_m, and α, as reported in **Figure 3.5A-C**. First, it is worth noting that Lipofectamine-driven transient expression of both LAMP1-GFP and CD63-EGFP yields clear structural alteration of lysosomes: a statistically significant average enlargement (1.6 folds, corresponding

to ~250 nm) of the organelle is found in both cases at 24 hours post-transfection, although with no consequences for lysosome dynamic properties (**Figure 3.5A-C**, full blue and green circles, respectively).

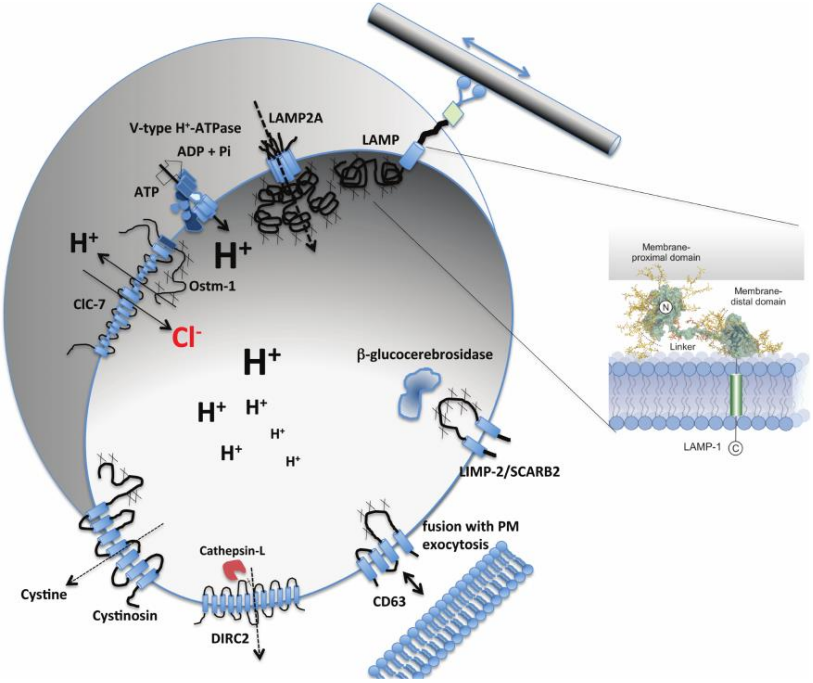

Figure 3.3 Schematic view of a lysosome and of the lysosomal membrane. *LAMP1 and CD63 proteins are specific lysosomal marker. CD63 was shown to be involved in fusion events with the plasma membrane. Both LAMP-proteins (LAMP-1 and LAMP-2) participate in autophagic pathways and it was proposed that they are also needed to control the motility of lysosomes though dynein-mediated transport along microtubules*[95]*. Image reprinted from ref.* [95]

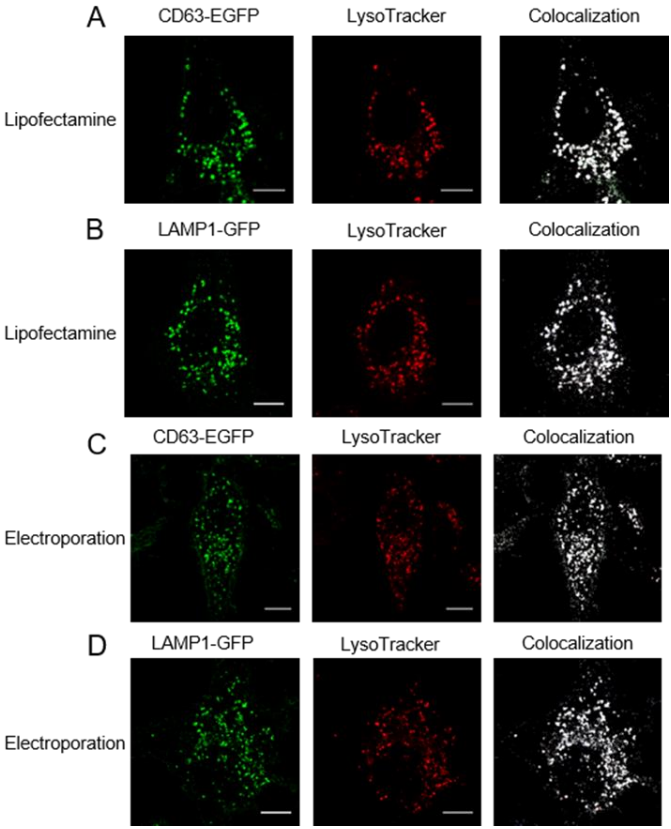

Figure 3.4 Co-localization assays. (A, B) *Confocal micrographs of HeLa cells expressing the lysosomal markers CD63-EGFP or LAMP1-GFP (both in green), transfected using Lipofectamine reagents, with lysosomes co-labelled with LysoTracker (in red), after 24 h of incubation with Lipofectamine-plasmid complexes.* ***(C, D)*** *Confocal micrographs of HeLa cells expressing the same lysosomal markers, but transfected using electroporation (lysosomes are co-labelled with LysoTracker, in red). Scale bars: 10 µm.*

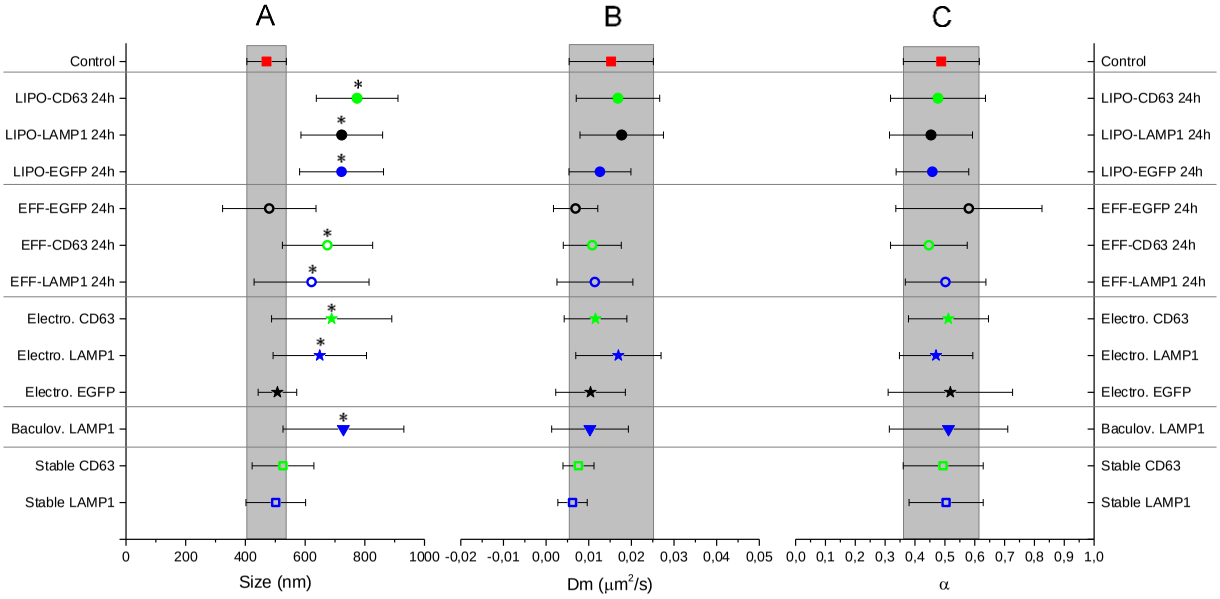
A
B
C
Control
LIPO-CD63 24h
LIPO-LAMP1 24h
LIPO-EGFP 24h
EFF-EGFP 24h
EFF-CD63 24h
EFF-LAMP1 24h
Electro. CD63
Electro. LAMP1
Electro. EGFP
Baculov. LAMP1
Stable CD63
Stable LAMP1
0 200 400 600 800 1000
Size (nm)
-0,02 -0,01 0,00 0,01 0,02 0,03 0,04 0,05
Dm (μm²/s)
0,0 0,1 0,2 0,3 0,4 0,5 0,6 0,7 0,8 0,9 1,0
α

Figure 3.5. (previous page) Statistical meta-analysis of lysosome structural and dynamic properties under different experimental conditions. *Mean ± SD values for size (**A**), D_m (**B**), and α (**C**) for all the conditions tested, which are detailed on the left and right axes. The '*' symbol indicates a Kolmogorov-Smirnov test with p≤0.001. The number of analyzed cells for each condition are reported in **Table 3.1**.*

A similar effect is produced even if the time of exposure to Lipofectamine reagents is reduced to 4 hours. Moreover, such structural alteration of the lysosome is irreversible, as no recovery is observed even after 48 hours of incubation in Lipofectamine-free medium. To test whether the lysosome structural alteration is caused by protein over-expression or by exposure to Lipofectamine reagents, an experiment was performed by the Lipofectamine-based transient expression of a lysosome-unrelated protein, i.e. untagged EGFP. Notably, Lipofectamine-driven expression of EGFP is associated with a clear enlargement of lysosomes (**Figure 3.5A**, full black circle), almost to the same extent as described for LAMP1-GFP and CD63-EGFP. This result prompted us to test additional transfection reagents/procedures. In particular, we used Effectene (as an alternative lipid-based, but non-liposomal, method) and cell electroporation (in which an external electrical field is applied in order to transiently increase the permeability of cell membranes). It is worth noting that both methods are not producing lysosome alterations, neither structural nor dynamic, if associated with untagged EGFP (**Figure 3.5A-C**, empty black circles and black stars, respectively). Quite

surprisingly, however, both methods induce lysosome alteration (~1.5-fold increase in size, but negligible effect on dynamics) if associated with the expression of the two lysosome protein markers, LAMP1-GFP and CD63-EGFP (**Figure 3.5A-C**, empty blue/green circles and blue/green stars). Taken together, these latter results, even if quantitatively similar to those obtained using Lipofectamine reagents, point to the effect of protein over-expression on the lysosome structural integrity. A number of additional control experiments and analyses were set to probe this hypothesis. First, two HeLa-based cell lines stably expressing either LAMP1-GFP or CD63-EGFP were generated in order to keep the recombinant protein expression at a minimum (see **Materials and Methods** for details). Notably, this was enough to recover the actual size of the lysosome (**Figure 3.5A**, empty blue and green squares, respectively), irrespective of the specific protein marker used.

3.2 Correlation between marker expression and lysosome size

At this point, in order to clarify whether lysosome structural alterations depend on the amount of protein accumulated on the

lysosome membrane, we quantified the mean fluorescence intensity (MFI) of the whole population of imaged lysosomes per each cell in our transient transfection experiments and correlated MFI to the *i*MSD readouts. The scatter plots in **Figure 3.6** - **Figure 3.9** show the results obtained for LAMP1-GFP expressed under different transfection protocols. It is anticipated here that similar results were obtained with CD63-EGFP. Interestingly, the plot in **Figure 3.6** clearly demonstrates that lysosome structural alteration under Lipofectamine treatment is independent of the protein final concentration obtained on the organelle membrane (i.e. no significant correlation between MFI and apparent lysosome size in LAMP1-GFP expressing cells is found, fit slope ~ 0).

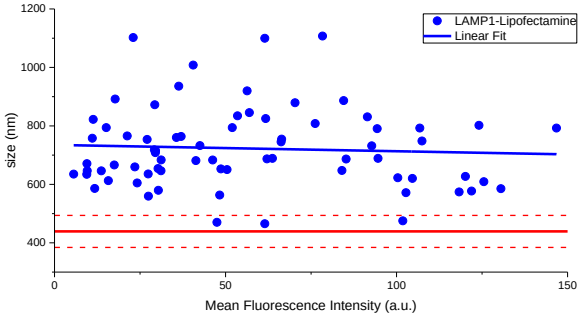

Figure 3.6 Effect of LAMP1-EGFP overexpression on lysosome structure. *Plots of lysosome average size vs MFI for LAMP1-EGFP positive lysosomes in cells transfected using Lipofectamine (full blue dots).*

By contrast, if LAMP1-GFP expression is triggered by Effectene- (**Figure 3.7**) or electroporation-based procedures **Figure 3.8**, a clear positive correlation is observed between the MFI and the extent of lysosome enlargement (fit slope>1): i.e. the higher the LAMP1-GFP expression level, the higher the average size of lysosomes.

Please note that low expression levels of LAMP1-GFP (lower-left portion of the plots in **Figure 3.7** and **Figure 3.8**) yield an average lysosome size close to that of the Lysotracker control (the y-axis intercepts of the linear fits correspond to ~420 nm for Effectene and ~520 nm for electroporation) and to that retrieved from stably-transfected cell lines (the range of observed MFIs for these latter is indicated in all plots by a grey vertical band).

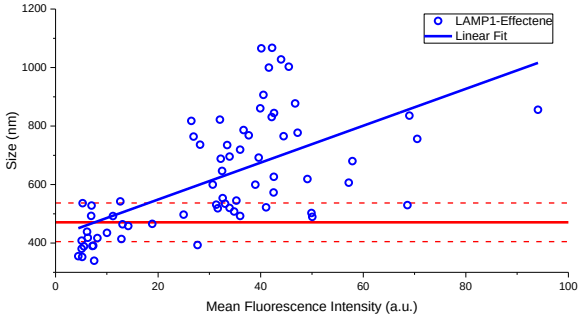

Figure 3.7 Effect of LAMP1-EGFP overexpression on lysosome structure. *Plots of lysosome average size vs MFI for LAMP1-EGFP positive lysosomes in cells transfected using Effectene (empty blue dots).*

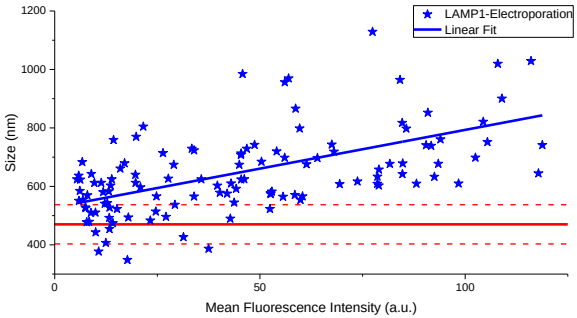

Figure 3.8 Effect of LAMP1-EGFP overexpression on lysosome structure. *Plots of lysosome average size vs MFI for LAMP1-EGFP positive lysosomes in cells transfected using electroporation (blue star).*

An additional, commercially-available, transfection tool was tested for LAMP1-GFP transient transfection, based on Baculovirus (**Figure 3.9**, see **Materials and Methods** for further details): the obtained results recapitulate what already discussed for Effectene- and electroporation-based experiments (y-axis intercept here corresponds to ~480 nm). Overall, reported results support the idea that Lipofectamine reagents may accumulate in the lysosome (as already recently observed by some of us [27]) causing persistent changes to the lysosome structural properties.

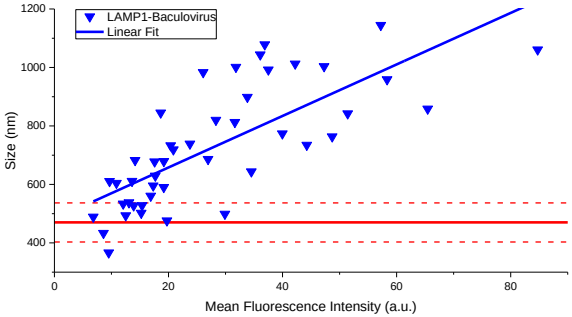

Figure 3.9 Effect of LAMP1-EGFP overexpression on lysosome structure. *Plots of lysosome average size vs MFI for LAMP1-EGFP positive lysosomes in cells transfected using Baculovirus (blue triangles)*

The alternative methods used, instead, are able to preserve lysosome structural identity, provided that recombinant protein expression is kept low. Regard to this latter result, a reasonable interpretation for the concentration-dependent deformation of the lysosome can be the steric hindrance due to multiple copies of either LAMP1-GFP or CD63-EGFP on the organelle membrane: both markers, in fact, contain transmembrane domains [94,96].

In conclusion, we unequivocally demonstrated here that Lipofectamine-based transient transfections lead to a substantial shift towards higher values of average lysosome size, irrespective of the fluorescent marker used (even if not lysosome-specific). This in turn suggests that the lysosome is highly sensitive to exposure to

Lipofectamine-DNA complexes, probably due to the accumulation of the lipidic component within the organelle. Most importantly, the lysosome alteration induced by Lipofectamine-based treatments can mask structural/dynamic alterations attributable to other causes (e.g. the overexpression of a lysosomal-specific marker, external stimuli, or even pathological conditions [19,97]). By contrast, Effectene- and electroporation-based strategies are able to preserve lysosome structural and dynamic identity, thus allowing to identify alterations due to other factors, as those mentioned above. In regard to this latter, we reported that the lysosome protein markers unavoidably alter the size of lysosomes in a concentration-dependent manner. This means that fine-tuning of their concentration (exclusively under the transfection conditions identified above) offers the possibility, in principle, to properly label the lysosome in live cells. These findings call into question the interpretation of a significant amount of previous data on labelled lysosomes from living cells, and suggests that multiple labeling strategies should be used to define their structural/dynamic properties.

CHAPTER 4

4. Lysosome structural and dynamic properties during NSCs differentiation

In this Chapter, the lysosome dynamics during the differentiation of neuronal stem cells (NSCs), obtained from mouse embryonic stem cells (mESCs), is investigated, in the cell soma, by means of iMSD. Single particle tracking (SPT), instead, allowed to properly characterized the organelle motion in all the cellular districts (included the projections) of the neuronal differentiating cell.

Most of the content of this Chapter was peer-reviewed and published with co-authors in:

- *Durso, W., Martins, M., Marchetti, L., Cremisi, F., Luin, S., & Cardarelli, F. (2020). Lysosome Dynamic Properties during Neuronal Stem Cell Differentiation Studied by Spatiotemporal Fluctuation Spectroscopy and Organelle Tracking. International journal of molecular sciences, 21(9), 3397.*

In this chapter, we investigated the lysosome dynamics during the differentiation of neuronal stem cells (NSCs), obtained from mouse embryonic stem cells (mESCs) differentiated using a protocol that mimics cortical development *in vitro* [98]. Embryonic stem cells (ESCs) are pluripotent cells with the capacity to renew themselves or to

differentiate into any of the three embryonic germ layers *in vivo* [99], and into the majority of cell types *in vitro* when subjected to the appropriate conditions. When mESCs are cultivated in chemically defined minimal medium (CDMM) and without external signals, they spontaneously undergo the entire process of neural differentiation from the very initial state [98,100,101]. Thus, the use of mouse ESC-derived NSCs allows to set up cultures of very early neural progenitor cells that would be very difficult to dissect from embryo. In order to control the specific neuronal type, it is possible to exploit Wnt (Wingless-related integration site), BMP (Bone morphogenetic protein), SHH (Sonic Hedgehog) and FGF (Fibroblast growth factor) signaling pathways [102], whose modulation is responsible for telencephalon regionalization *in vivo* [103]. In particular, inhibition of Wnt and Bmp signaling pathways at early stages of development is essential for the specification of the forebrain, and this was exploited to obtain developing cortical neurons [98].

In this model, *i*MSD was used to quantitatively address the vast population of lysosomes in the cell soma during the differentiation process. This analysis revealed a decrement in size of lysosomes with time, and modification of key dynamic parameters, such as the average local organelle diffusivity and anomalous coefficient; these changes

may parallel cytoskeleton remodeling during the differentiation process. SPT, on the other hand, allowed mapping heterogeneous dynamic responses of single lysosomes in different districts of the cells, and was the only analysis applied to movies done on projections, where only few organelles were imaged. SPT analysis highlighted a significant decrease of lysosomal transport in the soma followed by a rapid increase of transport in the projections at specific time points during neuronal differentiation, an observation compatible with the hypothesis that lysosomal active mobilization shifts from the soma to the newborn projections.

4.1 The biological system

In this study, to analyze lysosome dynamics in cortical neurons, we differentiate mESCs using the protocol described in details in [98] and in **Materials and Methods**. Briefly, we start from mESCs preconditioned with a medium containing Leukemia inhibitory factor (LIF) and two inhibitors (2i) of MAPK/ERK and glycogen synthase kinase 3b (GSK3b) pathways; these conditions make ESCs to express NANOG that allows the transcription of pluripotent genes and create a lenient chromatin structure.

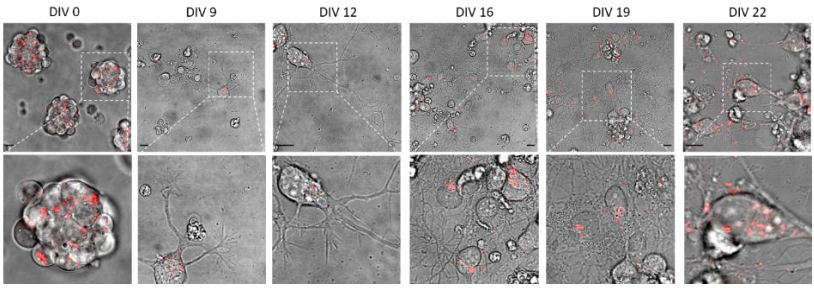

Figure 4.1 Microphotographs of living NSCs during differentiation, from DIV0 to DIV22. *Bright-field microscopy images (top) with the respective magnification of the area selected by the dashed line (bottom). The bright field images are all superimposed to a confocal fluorescence microscopy image (a section within somas) of lysosomes labeled with LysoTracker Red (in red). Scale bars: 10 μm.*

We are then able to mimic glutamatergic cortical neuron differentiation by administration of 53AH, a cyclohexyl analog of IWR-1 that selectively represses Wnt pathway. Together with Wnt inhibition, LDN193189 hydrochloride was used as a BMP inhibitor working through ALK2/3 (type I receptor serine-threonine kinases) and SMAD pathway inhibition [104]. Representative microphotographs of living mESC-derived NSCs during differentiation, from days in vitro (DIV) 0 to DIV22, are reported in **Figure 4.1**. In the top line of images, and especially in the zoomed images in the middle line, it is possible to appreciate the progressive formation of a neurites network. The bottom line of images, obtained by confocal fluorescence microscopy, shows how lysosomes can be observed thanks to labeling

with LysoTracker Red in the same field of view of the microimages in the first line.

4.2 iMSD analysis of lysosome dynamics during NSCs differentiation

In order to study lysosome dynamics during NSCs differentiation by means of *i*MSD, we first fast-imaged a subcellular region of interest within the cytoplasm (**Figure 4.2**).

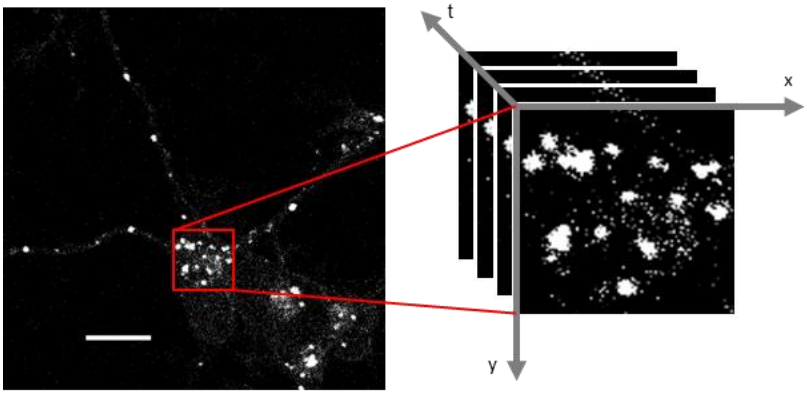

Figure 4.2 Confocal fluorescence microscopy image of a NSC shows the distribution of lysosomes labeled with LysoTraker Red. *Right: a stack of images from a sub-region of the image on the left are acquired with temporal resolution of 112 ms. Scale bar: 10 μm.*

*i*MSD traces from each acquisition were obtained through spatiotemporal correlation analysis. *i*MSD fitting then provided information related to average lysosome structural and dynamic properties. In particular, we extracted three parameters: (i) size (the square root of σ_0^2, y-axis intercept of the *i*MSD trace), proportional to the average organelle diameter, as previously demonstrated [87]; (ii) D_m, the local diffusivity, proportional to the initial slope of the (*i*)MSD; α, the anomalous diffusion coefficient (the exponent for a power-law fit, with offset, of the MSD), which has values close to, higher than, and lower than 1 for Brownian diffusion, super-diffusive, and sub-diffusive or confined motion, respectively. Differently from σ_0^2 and D_m, the α coefficient can be calculated on different temporal windows depending on the timescale of interest. Here, in particular, we calculate the α coefficient on two timescales: 15 seconds, for calculating the overall α coefficient, and below 1 second, for calculating the "α (short t)"; the latter is particularly useful to highlight the peculiar super-diffusive motion of lysosomes at a short timescale, if present [87].

We checked that the extracted parameters arise only from organelle motion and are not affected by overall cellular movements. These latter, according to the theory of spatiotemporal image correlation

spectroscopy [15,61], would appear as shifts in the position of the peak of the correlation function (which are not observed in our measurements).

Graphs in **Figure 4.3** show the *i*MSD plots from three exemplary movies at different neuronal differentiation times (DIV0, DIV5 and DIV22), and at two different time scales. As expected, at long time scale (14.6 s) *i*MSD graphs display an average sub-diffusive motion for the lysosomal populations ($\alpha = 0.47$ for DIV0, 0.57 for DIV5 and 0.34 for DIV22). On short time scale (0.8 s) *i*MSD plots reveal average super-diffusive or mostly Brownian behaviors for lysosomes ($\alpha = 1.4$ for DIV0, 1.2 for DIV5 and 0.94 for DIV22 in the examples of **Figure 4.3**). These results nicely match what we previously reported: a super-diffusive mode of motion emerges as a collective behavior at short spatiotemporal scales, while sub-diffusion dominates at longer spatiotemporal scales [87].

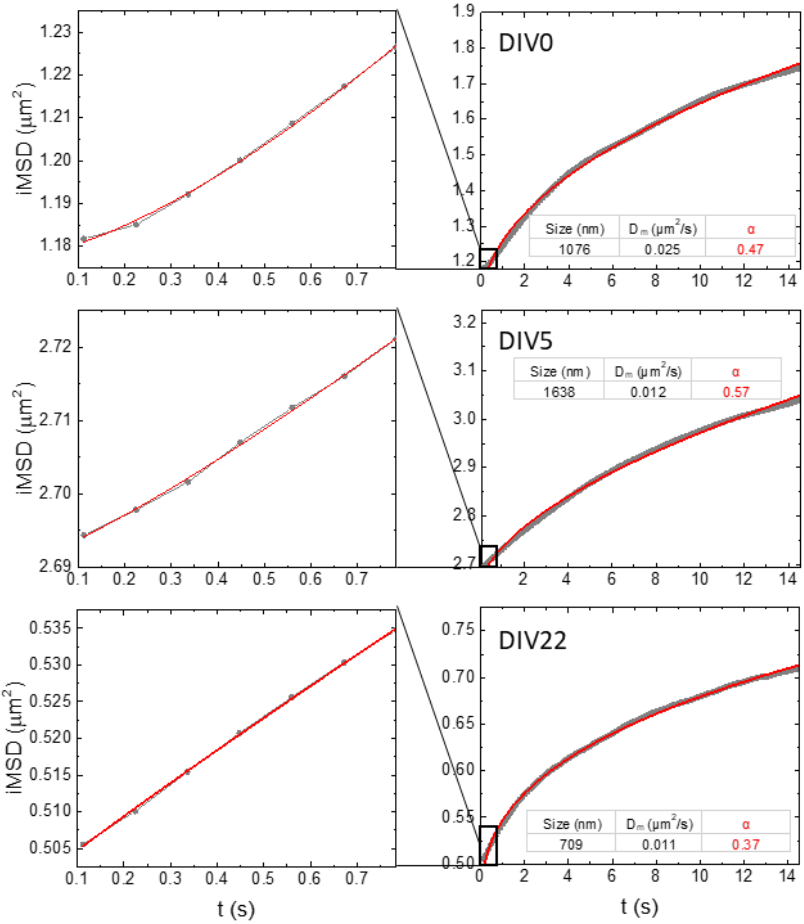

Figure 4.3 Exemplary iMSD plots obtained from imaging of living cells stained with LysoTracker at DIV0, 5 and 22 respectively. *Red traces: fits with a power law with offset. Right: long temporal scale (14.6 s). Left: short temporal scale (0.8 s).*

Figure 4.4 - Figure 4.8 report the average size, D_m and α coefficients extracted from *i*MSD plots of lysosomes inside the somas of NCSs throughout the entire neuronal differentiation process, with statistical analysis dedicated to highlight the differences in three exemplary time points of the process, DIV0, DIV4.5 and DIV22 (the post hoc Tukey test).

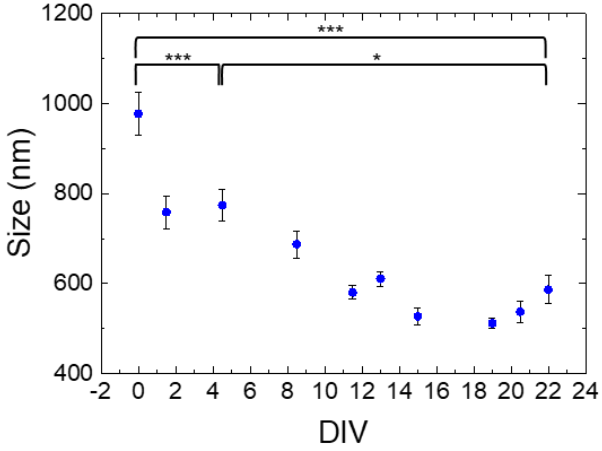

Figure 4.4 Plots of average size values extracted from iMSD analysis of NSC lysosomes populations acquired during differentiation (DIV0-22). *Error bars: Standard Error (SE). The population means of different time points are significantly different by one-way ANOVA ($p < 0.0001$). The results of the post hoc Tukey test are shown only for the comparisons amongst DIV0, 4.5 and 22; p-values: n.s. not significant, * <0.05; *** <0.001. Size average values with the respective DIV, N and SE are reported in* ***Table 4.1****.*

From a structural point of view, lysosomes display a significant decrement in size during neuronal stem cell maturation, from ~1 μm diameter at DIV0 to ~750 nm at DIV4,5 and, finally, to ~550 nm at the end of the differentiation protocol (DIV22) (**Figure 4.4**).

Such a progressive reduction of lysosome diameter during neuronal development might be the result of endosome maturation into lysosome, a process that in the neuronal cell occurs mostly in axons [105]. The restricted diameter of the emerging neuronal projection may act as "size filter" for the endosomes access to the maturation process. Furthermore, the observation that presynaptic biogenesis requires axonal transport of lysosome-related vesicles [106] corroborates this hypothesis.

Lysosome dynamics is subjected to modification during neuronal maturation, particularly in terms of local diffusivity. After a transient increase during the early phases of differentiation (with a maximum at 0.04 $\mu m^2/s$ around DIV5) D_m significantly decreases down to a plateau value of ~ 0.01 $\mu m^2/s$ at DIV13-to-DIV22 (**Figure 4.5**).

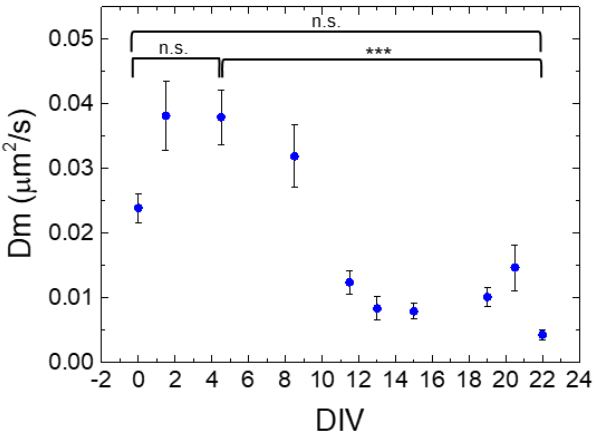

Figure 4.5 Plots of average Dm values extracted from iMSD analysis of NSC lysosomes populations acquired during differentiation (DIV0-22). *Error bars: Standard Error (SE). The population means of different time points are significantly different by one-way ANOVA ($p < 0.0001$). The results of the post hoc Tukey test are shown only for the comparisons amongst DIV0, 4.5 and 22; p-values: n.s. not significant, * <0.05; *** <0.001. Dm average values with the respective DIV, N and SE are reported in* ***Table 4.1****.*

Anomalous coefficient is less affected during the process. The α value displays a slight increase up to DIV13 (an increment Δα of ~0.2), then it decreases around the starting value (α ~ 0.5) (**Figure 4.6**). The transient increase of local diffusivity D_m and α anomalous coefficient of lysosome motion around DIV5 might reflect cytoskeleton remodeling towards a more organized structure [107]. Indeed, at DIV5, we observe a diffuse polymerization of actin filaments within the cells (**Figure 4.7D-F**).

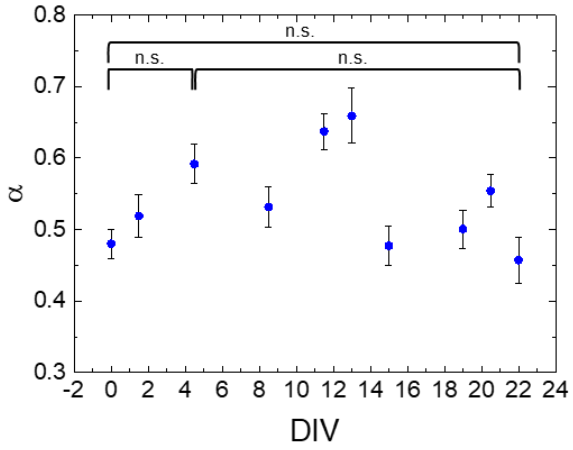

Figure 4.6 Plots of average α values extracted from iMSD analysis of NSC lysosomes populations acquired during differentiation (DIV0-22). *Error bars: Standard Error (SE). The population means of different time points are significantly different by one-way ANOVA ($p < 0.0001$). The results of the post hoc Tukey test are shown only for the comparisons amongst DIV0, 4.5 and 22; p-values: n.s. not significant, * <0.05; *** <0.001. α average values with the respective DIV, N and SE are reported in* ***Table 4.1****.*

When the cytoskeleton reaches a highly organized structure **(**DIV14, **Figure 4.7G-I**), the D_m drops to lower values, indicating a confinement exerted by the bundles of actin filaments on the organelles. A similar role of actin has been reported for the regulation of membrane mobility of selective membrane receptors [108]. The standard error (SE) associated to both the size and the local diffusivity becomes sensibly smaller during differentiation, probably reflecting an ongoing process by which the highly heterogeneous (both in size

and dynamics) population of lysosomes at DIV0 progressively becomes more homogeneous and acquires its final structural/dynamic identity in the fully differentiated cell.

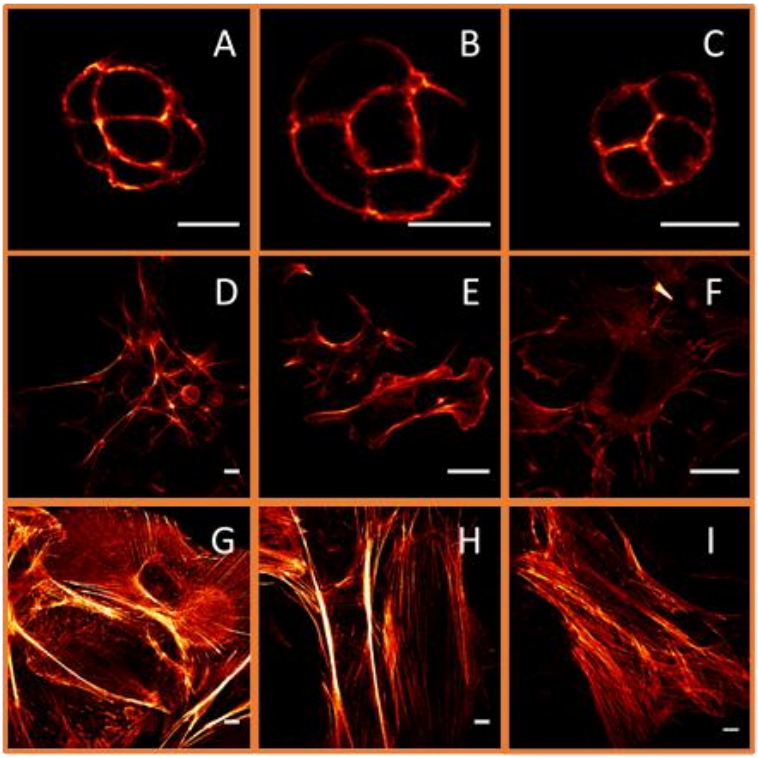

***Figure 4.7 Confocal images showing F-actin stained with Alexa Fluor™ 647 Phalloidin**. (**A, B, C**) DIV0 mouse embryonic stem cells (mESCs), at the beginning of cortical differentiation in medium without 2i and LIF. (**D, E, F**) Representative image of DIV5 mouse progenitor cortical neurons obtained by Wnt and BMP signaling pathways blockade in N2B27 medium. (**G, H, I**) Representative images of DIV14*

mouse cortical projection neurons maintained in neurobasal B27 medium. Scale bars in all images, 10 μm.

The α-parameter at short time scale (for t < 0.8 s), after an initial decreases from a maximum value of 1.17 (DIV0, more superdiffusive behavior) in the first days of differentiation, has then a more scattered behavior around 1, the value characterizing a mostly diffusive motion (**Figure 4.8**).

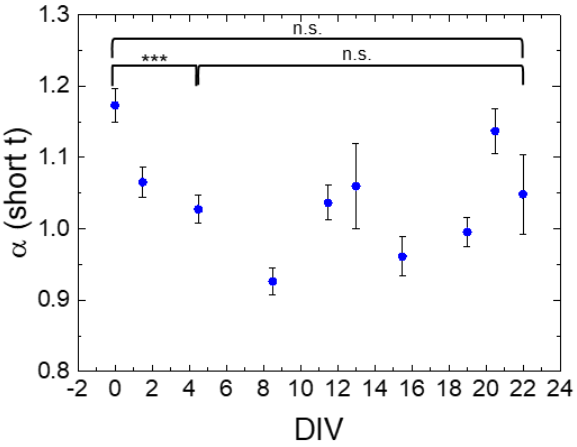

Figure 4.8 Plots of average α at short times values extracted from iMSD analysis of NSC lysosomes populations acquired during differentiation (DIV0-22). *Error bars: Standard Error (SE). The population means of different time are significantly different by one-way ANOVA (p < 0.0001). The results of the post hoc Tukey test are shown only for the comparisons amongst DIV0, 4.5 and 22; p-values: n.s. not significant, * <0.05; *** <0.001. α (short t) average values with the respective DIV, N and SE are reported in* ***Table 4.1****.*

Size				Dm			
DIV	**N total**	**Size**	**SE**	**DIV**	**N total**	**Dm**	**SE**
0	42	1006	81	0	42	0.023	0.003
1, 2	52	787	50	1, 2	52	0.037	0.009
4, 5	80	774	67	4, 5	80	0.038	0.006
8, 9	48	688	51	8, 9	48	0.030	0.008
11, 12	76	578	22	11, 12	76	0.012	0.003
13	35	611	20	13	35	0.008	0.002
15, 16	27	527	18	15, 16	27	0.008	0.001
19	70	512	18	19	70	0.010	0.003
20, 21	22	538	37	20, 21	22	0.015	0.005
22	18	587	31	22	18	0.004	0.001
α				**α short**			
DIV	**N total**	**α**	**SE**	**DIV**	**N total**	**α**	**SE**
0	42	0.49	0.04	0	74	1.17	0.02
1, 2	52	0.53	0.05	1, 2	68	1.07	0.02
4, 5	80	0.59	0.05	4, 5,6	111	1.03	0.02
8, 9	48	0.54	0.05	8, 9	70	0.93	0.02
11, 12	76	0.63	0.04	11, 12	97	1.04	0.02
13	35	0.66	0.06	13	33	1.06	0.06
15, 16	27	0.48	0.03	15, 16	52	0.96	0.03
19	70	0.50	0.04	19	93	1.00	0.02
20, 21	22	0.55	0.03	20, 21	29	1.14	0.03
22	18	0.46	0.03	22	21	1.05	0.06

Table 4.1 Average values of size, Dm, α and α at short times (α short) extracted from iMSD analysis of lysosomes during NSCs differentiation (DIV: day in vitro; SE: standard error).

For the parameter α at short time scale, the fits have been done for the first 7 points of the iMSD, and the results were considered valid only when the anomalous diffusion fit was better, with a confidence level above 95%, than a fit with a constant (F-test, with p-value of 0.05). One-way ANOVA test was performed in order to evaluate if the

population means of different time points for size, D_m, α and α (short t) were significantly different. Multiple comparisons were conducted using the *post-hoc* Tuckey test. The behavior of this parameter does not seem to reproduce the one observed for the previously discussed ones. However, it must be noted that this parameter can be calculated for most of the *i*MSD curves, also for the ones where the fit on the total curves is not appropriate (see number of observations in **Table 4.2**) because the *i*MSD has a non-monotonic (or not smooth enough) trend (see below).

Of particular note, since we observed the neurite outgrow at DIV12, the acquisitions of lysosomes in the neuronal projections started from this time-point. The analysis of lysosomes motion in the projections generated *i*MSD plots that did not correctly fit with the shifted power-law model we adopted to extract our parameters ($R^2 < 0.98$ and parameters with values outside reasonable bonds at long time scales, see the example in **Figure 4.9**). This might be due to: (i) an intrinsic limitation of the *i*MSD technique when used to analyze series of images with a low number of moving objects; and (ii) the high variability in the motion type and parameters displayed by the lysosomes especially in those regions. Indeed, one can notice few fast-drifting vesicles amongst mostly blocked, confined, or slowly

diffusing ones. Moreover, iMSD analysis is more influenced by the brighter vesicles in a movie, and we noticed that more confined vesicles are more often brighter, especially at later DIV and in the projections. In order to tackle more quantitatively these issues, we decided to apply a single particle tracking (SPT) approach.

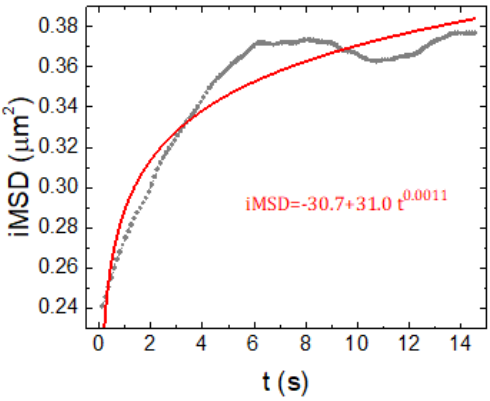

Figure 4.9 Representative iMSD plot of a neuronal projection at DIV12 (grey trace). *Red trace: shifted-power fit with R^2 = 0.91 and equation shown in red.*

4.3 SPT analysis of lysosome motion during NSCs differentiation

To properly characterize lysosome dynamics in all cell districts (cell body and projections), trajectories were extracted from some of the same movies used for iMSD analysis (**Figure 4.10**).

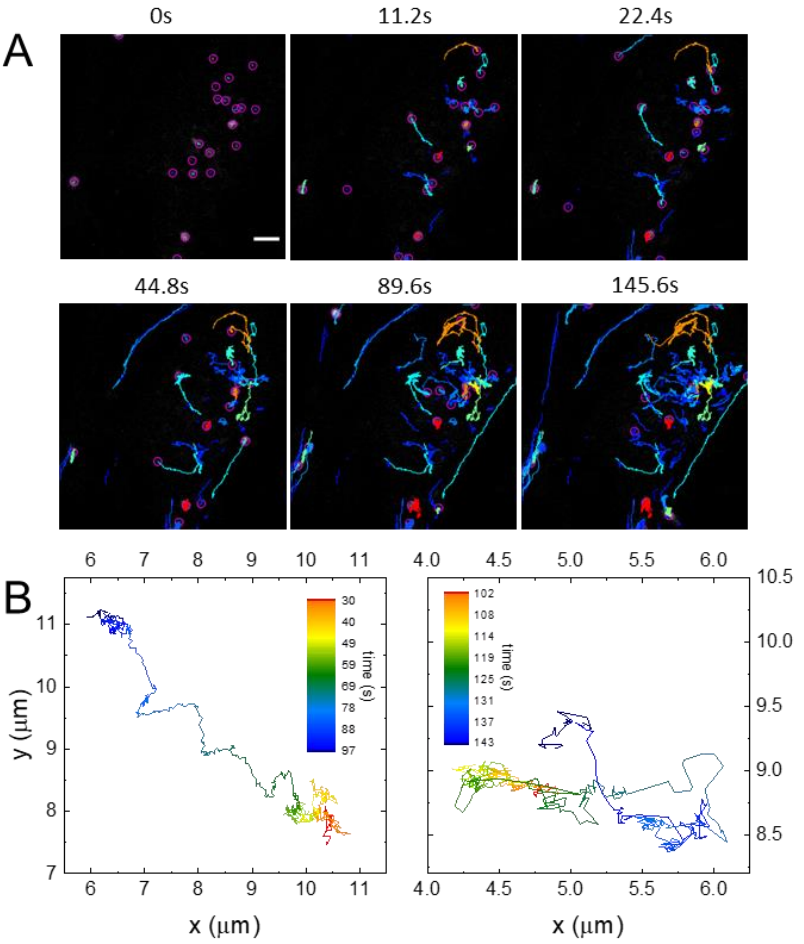

Figure 4.10 *(**A**) Representative images from time-lapse video of moving lysosomes within a differentiating NSC. Each colored trace represents trajectories travelled by different lysosomes. Scale bar, 2 µm. (**B**) Exemplary lysosome trajectory at DIV5. The color of the trajectory scales with time.*

Figure 4.10A exemplifies the very different types of motions undergone by the lysosomes, as described above. A more careful analysis of the trajectories reveals that this variability exists within the trajectories of single lysosomes (**Figure 4.10B**).

For the particle identification and the trajectory evaluation, we adopted TrackMate, a package in an open-source image-processing software (*i.e.* ImageJ), which provides the tools to perform single particle tracking (SPT). The adopted detector for the particle identification uses the Laplacian of Gaussians (LoG) approach and the tracking algorithm is based on a Linear Assignment Problem (LAP), which allows dealing with gap-closing events. The settings have been optimized without considering splitting and merging events. Different Matlab scripts were used to perform two consecutive analyses on the SPT-derived trajectories. The first step, fully described in [109], is based on the lysosome velocity (v) within a moving time-window of 5 frame: after a segmentation phase, trajectories or sub-trajectories with v above a definite velocity threshold (v_t) were considered as "drifted" ("go" motion as described in [109]). Other different parameters used here with respect to [109] are: minimum length for considering a trajectory: 15 frames; minimum length for subtrajectories, 4 frames; no minimum shift nor average velocity for including a trajectory in the analysis. The

non-drifted (sub-)trajectories, with average v below v_t, were analyzed by means of the Moment Scaling Spectrum (MSS) and Transient Arrest of Diffusion (TAD) as in [110,111]. This analysis allows further characterizing the organelle dynamics by quantifying the time spent by lysosomes in confined, diffusive or drifted motion. Within the "confined" category are included all the motion classified as "immobile", "slow", and "TAD events" in [110]; the "drifted" category includes the drifted subtrajectories as determined by both analysis steps. Parameters for TAD analysis different than in [110] are: time-window of maximum S_m=12 steps, probability level threshold L_c=2.0, minimal duration t_c of 6 steps for a transient confinement zone (TCZ); obtained (sub)trajectories were classified as in [110], with parameters optimized on the basis of careful inspection of present results in cell bodies and projections. The distributions (normalized to 100%) for time spent by lysosomes undergoing the various types of motion, and the relative uncertainties, were calculated similarly than in [112], where also the performed statistical test is described. Briefly, for each bin j (confined, diffusive, drifted) we summed the duration t_{ji} of each of the n_j (sub)trajectories i classified within j: the total time f_j and its variance $\sigma_{f_j}^2$ was calculated as $f_j = \sum_{i=1}^{n_j} t_{ji}$, $\sigma_{f_j}^2 = \sum_{i=1}^{n_j} t_{ji}^2 - \frac{\left(\sum_{i=1}^{n_j} t_{ji}\right)^2}{n_j}$. Differences were analyzed for significance using χ^2 tests, with the

statistic $\chi^2 = \sum_{k=1}^{N_p} \sum_{j=1}^{N} \frac{\left(f_j^{(k)} - E_j^{(k)}\right)^2}{\sigma^2_{E_j^{(k)}}}$ (k refers to the N_p compared distributions, $E_j^{(k)}$ is the expected value in the bin j with variance $\sigma^2_{E_j^{(k)}}$, N is the number of bins). This statistic follows a χ^2-distribution with $(N_p - 1)(N - 1)$ degrees of freedom; $E_j^{(k)}$ and $\sigma^2_{E_j^{(k)}}$ can be calculated by pooling together the data from the N_p populations.

In order to extract the fraction of time that the vesicles spend undergoing different motion, it was necessary to separate each trajectory in sub-trajectories with a single self-similar motion type. This was usually done in two steps: first, the longest, fastest and most directional drifted subtrajectories were extracted, similar to what was done in [109]. Then, the remaining trajectories (or parts of trajectories) were controlled for transient arrest of diffusion (TAD), and the obtained subtrajectories were classified as fast diffusing, slow/confined or blocked, and drifted, according to the parameters characterizing their motion (amongst which, short-time diffusivity *D* and anomalous diffusion coefficient α as in **Figure 4.5** and **Figure 4.6** respectively) as in [110,111]. The number of starting trajectories and obtained (sub)trajectories are reported in **Table 4.2**. The (relative) time that the lysosomes spent undergoing the different kinds of motion

were calculated by summing the duration of the various (sub)trajectories classified as above described. **Figure 4.11** reports these results across nine time points, from the embryonic stem cell stage (DIV0) to the mature neuronal cell (DIV22), and considering two velocity threshold for drifted subtrajectories in the first analysis step (v_t): v_t =1.0 μm/s, similar to the one chosen in [109], and v_t =0.5 μm/s (**Figure 4.11A** and **B** respectively). The difference between the two graphs is due to the peculiar vesicles dynamics, as explained later. Lysosome motion was measured in cell bodies at all time-points in the differentiation process, and from DIV12 to DIV22 in neuronal projections because they are not evident up to DIV9. In cell bodies, the early differentiation stage is characterized by an increase of both drifted and diffusive relative components, which reach a maximum at DIV5, with a consequent minimum in the "confined" category. After four days (DIV9), both drifted and diffusive relative fractions decrease and remains low to the last time point. Plots based on the evaluation with v_t 1.0 μm/s and 0.5 μm/s (**Figure 4.11A** and **B**, respectively) display similar behaviors, but with a usually higher impact of diffusive components if v_t=1.0 μm/s. *E.g.*, at DIV5 diffusive motion is undergone for 45% of time, while drifted and confined ones for 15% and 35% respectively; the same percentages are 14%, 27%, and 59% (diffusive, drifted, and confined) if v_t = 0.5 μm/s, instead. This can be

explained by looking closely at a trajectory considered “diffusive”, especially for v_t = 1.0 μm/s: often, it appears as composed by more slow or confined pieces connected by more drifted ones (**Figure 4.11B,** left), which are however too short or too slow to be recognized by either analysis step. Decreasing v_t allows to recognize more of these parts, therefore the (sub)trajectories initially considered diffusive are divided into confined and drifted subtrajectories.

In the projections, we can notice a similar behavior than in the soma compartments, but with less pronounced changes and delayed by ~10 days: drifted and diffusive relative fractions transiently increase with maximum at DIV15 and after seven days (DIV22) they decay to the starting value (**Figure 4.11**, empty symbols).

Overall, data coming from SPT analysis confirm that most of the analyzed lysosomes, both in the soma and in the projections, display a confined mode of motion regardless of the DIV investigated.

This is line with the iMSD data reported in **Figure 4.3** showing an average sub-diffusive dynamic behavior for the whole organelle population. However, we also unveil that lysosomal active transport within cell body has a transient but substantial increase at DIV5, which shows an intriguing correspondence in time to the increase in

expression of the neural progenitor marker *Sox1*, as measured by some of us [98] and others [113–115].

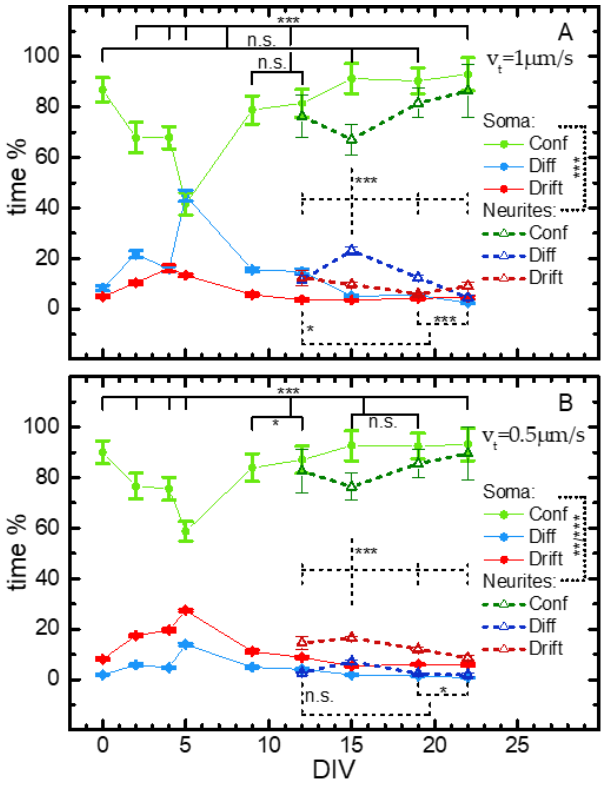

Figure 4.11 Dependence on DIV of the distributions (in %) for the time spent by lysosomes in confined (Conf), diffusive (Diff) and drifted (Drift) motion during neural differentiation, within cell bodies (DIV0-22, dots and solid lines) and projections (DIV12-22, triangles and dashed lines). *Velocity threshold for drifted subtrajectories in the first analysis step (see text) vt = 1.0 µm/s (**A**) and 0.5 µm/s (**B**). The differences at different DIVs are very highly significant (p<10-20) within each*

*case (soma or projections) according to a χ^2 test (see materials and methods for tests and uncertainties). Soma and dendrites are highly significantly different at each considered DIV. (Bonferroni-adjusted) p-values for single comparisons: n.s. >0.05; * <0.05; ** <0.01; *** <0.0015. All the statistical data for this graphs are reported in* ***Table 4.2****.*

Then a dramatic decrease of lysosomal transport in the soma (DIV9) is followed by a rapid increase of transport activation of lysosomes in the projections at DIV15. The latter could be less pronounced than in the soma, as a result of not perfect synchronization between the outgrowth of different neurite processes. Our observations are compatible with the hypothesis that lysosomal active mobilization shifts from the soma to the newborn projections. Interestingly, a distal accumulation of signaling endosomes transporting neurotrophic factors was recently found in the elongating axons of neurons [116]. It is thus tempting to hypothesize that the distal mobilization of lysosomes may as well support the elongation process, possibly contributing to presynaptic biogenesis [106].

4.4 Conclusions

Here we studied lysosome dynamics during NSCs differentiation using two different but complementary approaches: a population-based method (*i*MSD) and a single-objects-method (SPT). Our results

provide new insight on the lysosome dynamics throughout NSCs differentiation, supporting new functions proposed for this organelle and opening to new studies on the pathophysiological role of lysosome and lysosome-related organelles in human health and disease. The differential activation of lysosomal transport between cell body and projection matches the emerging idea of lysosome as a signaling hub [70]. Recent evidences, furthermore, suggest that lysosomes might participate in local axonal translation [117]: mRNA granules, in fact, hitchhike on lysosomes for axonal transport [118]. Therefore, a better comprehension of lysosomal biophysics could shed new light on the relationship between gene expression and synaptic activity.

			v_t=1.0 μm/s					v_t=0.5 μm/s				
sample	trajs	type	time (s)	Δ time (s)	time %	Δ time %	(sub)trajs	time (s)	Δ time (s)	time %	Δ time %	(sub)trajs
DIV0	952	Conf	14609	795	86.8	4.7	966	15109	771	90.0	4.6	1182
		Diff	1392	167	8.3	1.0	198	316	21	1.9	0.1	124
		Drift	821	74	4.9	0.4	357	1359	73	8.1	0.4	1258
		TOT	16823	816	100.0	4.8	1521	16785	775	100.0	4.6	2564
DIV2	595	Conf	4600	407	67.9	6.0	477	5151	342	76.7	5.1	900
		Diff	1472	93	21.7	1.4	255	394	25	5.9	0.4	176
		Drift	704	45	10.4	0.7	493	1174	30	17.5	0.5	1422
		TOT	6776	420	100.0	6.2	1225	6719	345	100.0	5.1	2498
DIV4	967	Conf	4057	265	67.9	4.4	776	4500	269	75.6	4.5	1011
		Diff	947	62	15.8	1.0	243	284	21	4.8	0.3	142
		Drift	969	70	16.2	1.2	617	1169	37	19.6	0.6	1212
		TOT	5973	281	100.0	4.7	1636	5953	272	100.0	4.6	2365
DIV5	607	Conf	2998	317	41.6	4.4	539	4216	279	58.7	3.9	1081
		Diff	3236	159	44.9	2.2	570	999	39	13.9	0.5	452
		Drift	967	38	13.4	0.5	988	1968	33	27.4	0.5	2576
		TOT	7202	356	100.0	4.9	2097	7183	283	100.0	3.9	4109
DIV9	766	Conf	10797	775	78.9	5.7	762	11452	740	83.9	5.4	1097
		Diff	2118	114	15.5	0.8	339	672	47	4.9	0.3	233
		Drift	775	80	5.7	0.6	516	1519	82	11.1	0.6	1642
		TOT	13690	787	100.0	5.8	1617	13644	746	100.0	5.5	2972
DIV12 (soma)	680	Conf	10629	723	81.5	5.5	892	11321	708	87.1	5.4	1048
		Diff	1940	129	14.9	1.0	274	534	35	4.1	0.3	176
		Drift	478	66	3.7	0.5	302	1146	55	8.8	0.4	1264
		TOT	13047	738	100.0	5.7	1468	13001	711	100.0	5.5	2488
DIV15 (soma)	699	Conf	11647	762	91.3	6.0	670	11822	761	92.7	6.0	826
		Diff	661	63	5.2	0.5	114	248	25	1.9	0.2	80
		Drift	454	36	3.6	0.3	214	686	33	5.4	0.3	683
		TOT	12762	765	100.0	6.0	998	12756	762	100.0	6.0	1589
DIV19 (soma)	816	Conf	18970	1089	90.4	5.2	967	19389	1051	92.5	5.0	1165
		Diff	1140	89	5.4	0.4	163	318	29	1.5	0.1	108
		Drift	884	94	4.2	0.4	427	1258	65	6.0	0.3	1234
		TOT	20994	1097	100.0	5.2	1557	20965	1053	100.0	5.0	2507
DIV22 (soma)	635	Conf	12724	891	93.0	6.5	700	12715	890	93.1	6.5	721
		Diff	329	28	2.4	0.2	91	109	13	0.8	0.1	55
		Drift	628	79	4.6	0.6	241	827	80	6.1	0.6	536
		TOT	13681	895	100.0	6.5	1032	13651	893	100.0	6.5	1312
DIV12 (proj.)	183	Conf	3903	435	76.3	8.5	372	4208	439	82.6	8.6	359
		Diff	582	108	11.4	2.1	68	141	15	2.8	0.3	57
		Drift	633	154	12.4	3.0	204	746	136	14.6	2.7	527
		TOT	5118	474	100.0	9.3	644	5094	460	100.0	9.0	943
DIV15 (proj.)	481	Conf	6229	559	67.1	6.0	555	7060	493	76.4	5.3	1015
		Diff	2149	154	23.2	1.7	271	659	54	7.1	0.6	189
		Drift	906	63	9.8	0.7	584	1527	57	16.5	0.6	1566
		TOT	9284	583	100.0	6.3	1410	9246	499	100.0	5.4	2770
DIV19 (proj.)	551	Conf	11474	830	81.6	5.9	771	11973	781	85.5	5.6	1181
		Diff	1758	101	12.5	0.7	277	337	27	2.4	0.2	134
		Drift	837	44	5.9	0.3	669	1691	81	12.1	0.6	1786
		TOT	14069	837	100.0	5.9	1717	14001	786	100.0	5.6	3101
DIV22 (proj.)	205	Conf	3977	491	86.4	10.7	261	4117	482	89.5	10.5	271
		Diff	208	34	4.5	0.7	47	84	28	1.8	0.6	27
		Drift	419	68	9.1	1.5	142	397	46	8.6	1.0	315
		TOT	4604	497	100.0	10.8	450	4598	485	100.0	10.6	613

***Table 4.2 (previous page) Statistical data for Figure 4.11**. The total duration (time) of trajectories classified as undergoing a distinct type of motion (Conf: confined; Diff: diffusive; Drift: drifted) are reported for all observed DIV (days in vitro) in somas (soma) and projections (proj.), together with their uncertainties (Δ time) and their percentages (%) with respect to the reported totals (TOT). We report also the starting number of trajectories (trajs) and the final number of trajectories and/or subtrajectories [(sub)trajs] after the two steps of trajectory segmentation; the comparison of these numbers can give an idea of the heterogeneity of motion amongst and within single lysosome trajectories. vt: velocity threshold in the first step of trajectory segmentation (see main text).*

CHAPTER 5

5. Conclusions and future perspectives

In this Thesis, the *i*MSD correlative-based technique is proposed as a quantitative tool to address the characteristic structural and dynamic properties of sub-cellular, dynamic and nanoscopic compartments in living cells. Starting from a standard stack of images in time, collected with the proper scanning frequency, the *i*MSD algorithm affords simultaneous access to several important parameters of the diffusing object of interest, such as its average size, diffusivity, and overall mode of motion.

The properties and advantages of *i*MSD are evident if compared to the techniques currently available to retrieve analogous information. With respect to structural information, the preferred choice is transmission electron microscopy (TEM) analysis. By this imaging method, ultrastructural details at molecular resolution (and even beyond) can be retrieved, also at the level of subcellular nanostructures. Yet, the peculiar spatial resolution of TEM is achieved at the expenses of the information in the temporal dimension, which is inevitably lost due to the required chemical-fixation procedures. To compensate for this, the

recent advances in live-cell imaging technologies are of particular interest here. On one side, these include the availability of new fluorescent markers with increased performances (e.g., brightness and photo-stability), optimized labeling procedures, and more sensitive detectors. In addition, analytical tools were developed to address both the structural (e.g., 'size' by phasor-based analysis of local image correlation spectroscopy, PLICS [21], aggregation/oligomerization by Number&Brightness analysis [119]) and dynamic (e.g., diffusion law by single-particle tracking (SPT) [22–27]) properties of objects of interest at the subcellular scale. The SPT method, for instance, affords direct access to the object trajectory and its classical MSD. However, the disadvantage is the need for a low density of the probe and very bright labels. Also, many single-object trajectories are to be measured to satisfy statistical criteria. With respect to the temporal resolution of the measurement, inorganic, photostable probes (e.g., quantum dots or metal nanoparticles) can increase SPT performance but at the expense of complex production/labeling procedures.

Compared to these standards, the *i*MSD method shows some key advantages. First, this approach can be used in conjugation with relatively dim fluorescent tags, such as genetically encoded fluorescent proteins. Thus, compared to SPT, a higher temporal

resolution is achieved (using the same label) due to the lower amount of photons required. Second, the *i*MSD method is not limited by diffraction but only by the temporal resolution available. In fact, in spite of the diffraction-limited optical setup used, average molecular displacements even below the diffraction limit can be measured, as already demonstrated for molecular flows by using STICS [15]. The actual resolution in the measurement of displacements depends on how accurately (in terms of signal to noise) the correlation function can be measured, thus explaining why it is not limited by diffraction. Thus, it appears clear that the minimum displacement that can be measured depends on the diffusivity of the object of interest and on the temporal resolution of the imaging setup.

In this regard, it is important to consider that application to subcellular nanostructures, such as the lysosomes reported in this Thesis, appears optimal: in fact, the scanning-speed typically available in standard setups is significantly higher than the dynamics of the subcellular object of interest. In such a case, the movement of the objects during the acquisition are negligible, and the correlation function can be approximated by a Gaussian function. Finally, the *i*MSD approach can be easily applied to a wide range of commercial optical microscopy setups based both on raster scan or wide-field camera-based imaging,

with no need for system calibration (required only if an accurate estimate of particle size is to be achieved). An important parameter for the method to work is proper spatial sampling. As a general rule, to reach satisfactory convergence of the fitting algorithm, the minimum size of the region of interest for imaging should be at least 3-times larger than the maximum displacement of interest.

Overall, the *i*MSD approach must be considered as a tool to get rapid access to information at the whole-cell level, thus particularly suited to large-scale screening applications. At the same time, the inherent simplicity, robustness, and modest dependence on labelling strategies (and on S/N ratio) opens the way to straightforward additional applications. For instance, *i*MSD might be used to recognize and quantitatively describe average alterations in the properties of a particular subcellular structure of interest occurring, for instance, under pathological conditions. Derailed endocytosis commonly found in cancer cells [4,5], altered granule trafficking is found in β-cells exposed to Type-2-Diabetes-mimicking conditions [18], enlarged lysosomes packed with twisted microtubules observed in globoid cell leukodystrophy or galactosylceramide lipidosis [19], abnormalities in the endosomal-lysosomal system occurring in neurodegenerative diseases, especially Alzheimer's disease (AD) [20], are just few

examples. Moreover, *i*MSD might be also used to obtain the dynamic fingerprint of selected sub-cellular structures as a reference for testing the time evolution of the intracellular trafficking of exogenously added compounds, such as nanoparticles coated by biomolecular corona [120], drug-delivery vectors [121], pathogens, sensors, etc., in analogy with the macropinosome example reported in Chapter 2. In general, this approach allows for the real-time characterization of the intracellular evolution of the trafficking process and offers a simplified experimental scheme (only one species labelled, one detection channel, and no additional data analysis to retrieve co-localization coefficients). At the same time, it is fully compatible with virtually any kind of imaging modality, from camera-based (e.g. TIRF, SPIM) to scanning-based systems (e.g. confocal, STED-based imaging), from 1- to multi-photon excitation, etc., the only requisite being that the time resolution of the measurement can be properly tuned to the characteristic dynamics under study. All these implementations could transform the *i*MSD technique in a flexible, multiplexed platform to address quantitatively the complex regulation of life at the subcellular level. Related to this, it is envisioned that cross-*i*MSD analysis will be used in the near future to select subpopulations of subcellular nanostructures and reveal their

interactions and co-diffusion within the cell (this latter being a hot topic in cellular biophysics) by a multi-channel experiment.

If any detail is lost by *i*MSD analysis, this is certainly related to the large amount of molecular information enclosed within dynamic subcellular nanostructures. Such information is inevitably averaged out during the measurement due to poor temporal resolution. Theoretically, however, there is no technical limit to the possibility to retrieve molecular information, provided that sufficient acquisition speeds can be achieved. Due to the continuous improvements in detector speed/sensitivity and imaging technologies, it is envisioned that information about the whole subcellular compartment and its molecular constituents will be extracted from a single dataset.

In this regard, Di Rienzo et al. proposed a simulated experiment in which fluorescent molecules can move within a vesicle that is comparable in size to the static spatial resolution of the measurement [122]. The simulated image series is used to reconstruct the *i*MSD profile of fluorescent molecules. **Figure 5.1** shows that, by means of spatiotemporal fluorescence correlation spectroscopy, one can access the motion of fluorescent molecules trapped within moving vesicles and thus fully exploit information collected on timescales up to microseconds. More in detail, the *i*MSD plot shows two different

diffusive regimes: a short-range diffusion representative of the motion of molecules within the vesicles, and 10-fold slower, long-range diffusion that reflects the movement of the entire vesicle.

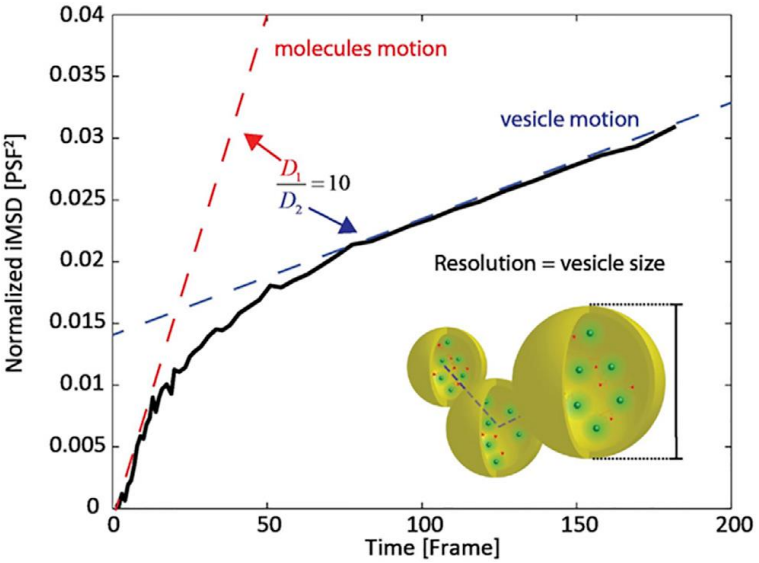

Figure 5.1 iMSD-based analysis can super-resolve single molecule dynamics: a simulated experiment. *A three-dimensional moving spherical object (in this case, a vesicle) with a diameter corresponding to the nominal measurement resolution (PSF) is filled with fluorescent molecules (see drawing in the inset). Both the vesicle and the molecules are free to diffuse, but the latter are 10 times faster than the vesicle and cannot cross the imposed spherical boundary. By applying spatiotemporal analysis of fluorescence fluctuations, one can measure the motion of the molecules within the vesicle (red dashed line) and the motion of the vesicle (blue dashed line) concomitantly, even if both are significantly smaller than the nominal imaging resolution. Image adapted from ref.* [122]

In this regard, preliminary experiments are in due course in our laboratory to demonstrate the feasibility of fast imaging to recover molecular information, with promising results. In particular, again we focused on lysosomes as paradigmatic organelles: HeLa cells were transfected with GFP-CD63 expression plasmids (see Chapter 3 and Appendix, Material and Methods) and stacks of images at 33 nm of pixel size were collected under a confocal microscope at different sampling times (**Figure 5.2A** and **B)**. Acquisitions were done at 2, 4, 8, 20, 40, 100 and 200 µs of pixel dwell time and data were analyzed using RICS and STICS. **Figure 5.2C** shows the comparison between the diffusion coefficients of Lysotracker inside lysosomes and CD63 on the external surface of lysosomes obtained at 2 µs pixel dwell time. Lysotracker molecules inside lysosome move faster than protein on its external surface (**Figure 5.2D**).

To provide additional support to the reliability of this application, we again conducted the analysis on lysosomes, but on a pathologic condition which impairs this particular organelle, the Krabbe disease. Krabbe disease is an autosomal recessive disorder caused by a deficiency of galactocerebrosidase (GALC) activity in lysosomes leading to accumulation of galactoceramide and neurotoxic

galactosylsphingosine (psychosine) in macrophages and neural tissue leading to progressive loss of myelin [123].

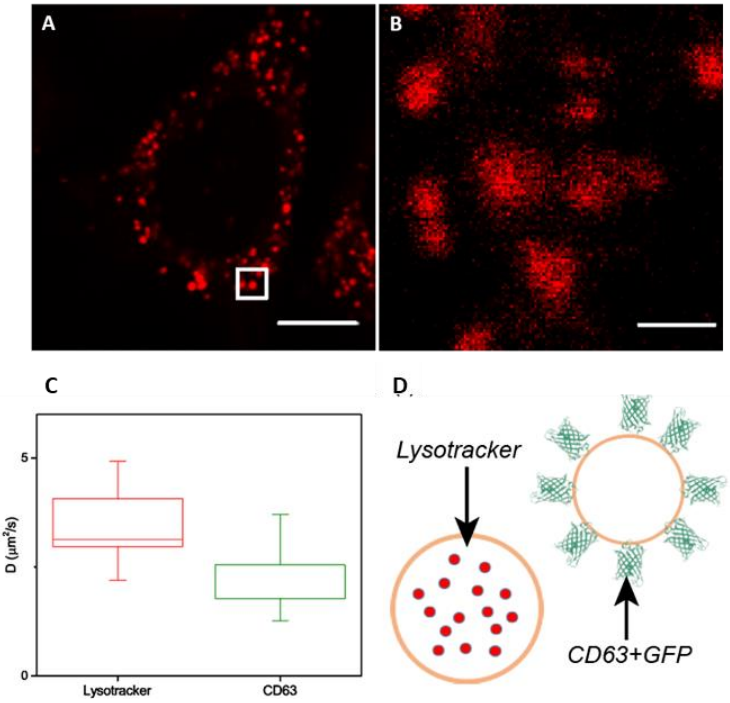

Figure 5.2 Diffusivity of Red Lysotracker and GFP-labelled CD63. *(**A**) Confocal image of a HeLa cell labelled with Red Lysotracker (scale bar 10 μm). (**B**) Magnification of figure A, white square. This is the magnification used for time-tunable RICS experiments (i.e., 33 nm per pixel). (**C**) Plot of the diffusion coefficients of Red Lysotracker (red) and GFP-labeled CD63 (green) measured on lysosomes of HeLa cells obtained at 2 μs of pixel dwell time. Upper and lower edges of the boxes represent the 25 and 75 percentile of the distributions found, the middle line shows the mean value. Whiskers show standard deviations. (**D**) Schematic representation of the two distinct situations.*

The Twitcher mouse is widely used as an animal model for Krabbe disease, also resulting from a mutation in the GALC gene. The biochemical and neuropathological findings in Twitcher as well as the clinical course of the disease closely resembles that observed in humans with Krabbe disease [124]. As a preliminary test, we measured the diffusion coefficients of Lysotracker inside lysosomes of fibroblast cells harvested from Twitcher mice. Lysosomes of Twitcher cells were analyzed using time-tunable RICS with the following parameter settings: stacks of images at 33 nm of pixel size were collected under a confocal microscope at different sampling times; acquisitions were performed at 2, 4, 8, 20, 40, 100 and 200 µs of pixel dwell time and data were analyzed using RICS and STICS algorithms. In parallel, WT fibroblasts were used as a control. As reported in **Figure 5.3**, Lysotracker showed lower diffusion coefficients inside lysosomes of Twitcher cells (blue dots) when compared to the WT case. For the Stoke-Einstein equation, this automatically translates into a higher viscosity of lysosomes in Twitcher cells. **Figure 5.4** shows the statistics of diffusion coefficients obtained at 2 µs per pixel-dwell-time. Lysosomes of WT cells showed an average diffusion coefficient two times higher than those measured in Twitcher cells, in agreement with the results presented by Devany et al.[125], using a different approach, on lysosome viscosity.

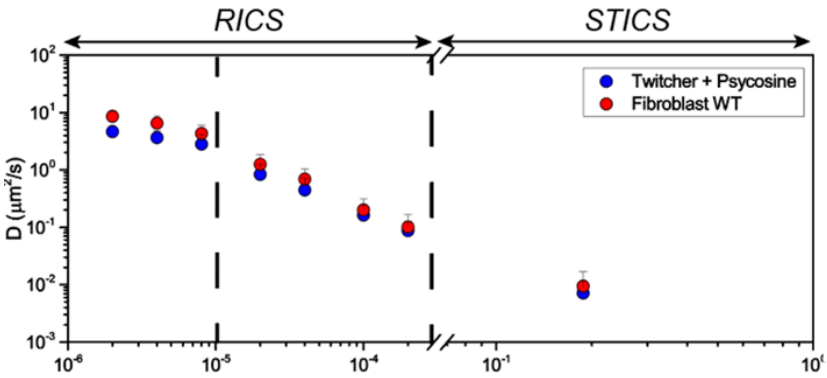

Figure 5.3 Diffusivity of Red Lysotracker in lysosomes of Twitcher fibroblast treated with Psycosine. *This graph shows the Diffusion coefficients found for both Twitcher Fibroblasts treated with Psycosine (blue dots) and Wild Type Fibroblasts (red dots) at different sampling time. Note the distinction between RICS and STICS time domains. Notice how Twitcher cells show, in general, lower diffusion coefficients, thus resulting in a more viscous environment compared to WT case.*

On one side, I envision that future investigations shall move towards a biophysical analysis of lysosome structural and dynamic properties during the differentiation of NSCs in the Twitcher mouse model by means of the *i*MSD-SPT combined approach, analogously to what reported in **Chapter 4**.

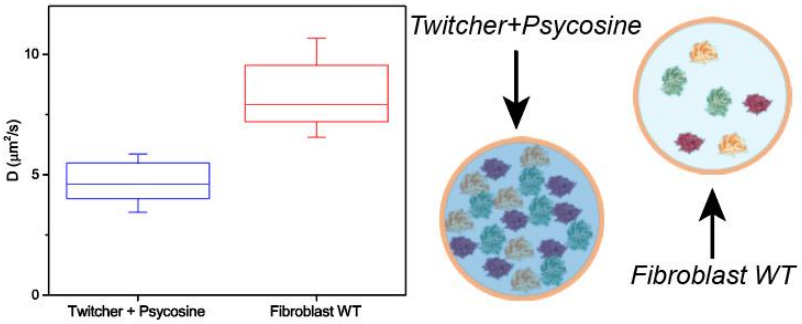

Figure 5.4 Diffusion coefficients of Red Lysotracker inside the lumen of Twitcher cells treated with Psycosine compared to WT cells. *Plot of the diffusion coefficients of Twitcher Fibroblast treated with Psycosine (blue) and Wild Type Fibroblast (red) measured on lysosomes of HeLa cells obtained at 2 μs of pixel dwell time. Upper and lower edges of the boxes represent the 25 and 75 percentiles of the distributions found, the middle line shows the mean value. Whiskers show standard deviations (left side). Schematic representation of the two distinct situations (right side). The mean value of the diffusion coefficient of WT cells almost doubles the value of the Twitcher case.*

On the other hand, the approach should be integrated with fluctuation analysis at time-tunable scales, as showed in the preliminary results of this Chapter, to retrieve information on the molecular scale. In my opinion, such an comprehensive approach have the potential to better dissect the physiopathology of Krabbe disease (as well as that of other targets in nanomedicine) at the relevant spatiotemporal scales.

APPENDIX

I. Materials and Methods

i. Cell culture and treatments

HeLa cells (CCL-2 ATCC) were cultured in Dulbecco's modified eagle medium (DMEM) low glucose (1g/L) without phenol red (Gibco), supplemented with 10% fetal bovine serum (FBS, Gibco), 100 U/mL of penicillin, and 100 µg/mL of streptomycin in a humidified incubator at 37 °C and 5% CO_2. Cells were seeded on 22-mm glass bottom dishes (WillCo Wells) and allowed to adhere overnight in a 37°C and 5% CO_2 cell culture incubator. CellLight Early Endosomes-GFP BacMam 2.0 (Invitrogen) and CellLight Late Endosomes-GFP BacMam 2.0 (Invitrogen) were used to mark early and late endosomes, respectively. Cells were transduced with CellLight reagents according to the manufacturer's instructions. Briefly, cells were incubated with 40 µl of the CellLight solution with baculovirus in full growth medium overnight at 37 °C and 5% CO_2. LysoTracker Red DND-99 (Invitrogen) stock solution was diluted to 60 nM final concentration in the growth medium. The medium from

the dish was removed and pre-warmed (37°C) probe-containing medium was added. Cells were incubated for 20 minutes and then observed. Transferrin from Human Serum conjugated to Alexa Fluor® 488 (Invitrogen) was used to label clathrin-mediated endocytosis. Transferrin conjugate was reconstituted in phosphate buffer saline (PBS) to obtain a 0.1 mM stock solution. Cells were incubated in a medium containing 20 nM of transferrin conjugate at 37 °C for 20 minutes then the medium was replaced. To investigate caveolae, cells were transfected with Caveolin-E[1]GFP by electroporation using Neon Transfection System 100 µL Kit (Invitrogen). Cells were trypsinized, pelleted, and resuspended in Resuspension Buffer R. DNA (15 µg) was added to 1×10^6 cells in 220 µL buffer, followed by electroporation using Neon Transfection System (Invitrogen) operating at a voltage of 1005 V and width of 35 ms. The cells were then seeded and cultured in DMEM containing 10% FBS and supplements without antibiotics and used in experiments 24 h later. Fluorescein isothiocyanate-Dextran 70 kDa was used to label macropinosomes. Cells were washed three times with PBS, then the medium was substituted with Dextran-containing medium (1 mg/ml) and incubated at 37 °C for 30 minutes. At the end of the incubation period, cells were washed three times and the medium replaced. Microtubule depolimerization was induced by

incubating the cells with 10 µM Nocodazole for 20 minutes and then washing with PBS before imaging.

Murine ES cell lines E14Tg2A (passages 35-40) were cultured and neuralized essentially as described [98], with minor modifications. For ES cell expansion, cells were grown on gelatin-coated tissue culture dishes (pre-treated 10' with 0.1% gelatin in PBS) at a density of 40000 cells/cm^2. ES cell medium, changed daily, contained GMEM (G5154, Sigma-Aldrich), 10% Fetal Calf Serum (12133C, Sigma-Aldrich; FCS), 2mM Glutamine (25030, ThermoFisher Scientific), 1mM sodium Pyruvate (25030, ThermoFisher Scientific), 1 mM non-essential amino acids (NEAA, 11140, Sigma Aldrich), 0.05 mM β-mercaptoethanol (M3148, Sigma Aldrich), 100 U/ml Penicillin/Streptomycin (15140, ThermoFisher Scientific) and 1000 U/ml recombinant mouse LIF (PMC9484, TermoFisher Scientific). Before starting the differentiation protocol, cells were passaged three times in 2i + LIF medium, in which FCS is substituted by two chemicals: PD0325901 (Sigma) and CHIR99021 (Sigma), which work as two inhibitors (2i) of MAPK/ERK and glycogen synthase kinase 3b (GSK3b) pathways, respectively. Chemically defined minimal medium (CDMM) for neural induction consisted of DMEM/F12 (21331-046, ThermoFisher Scientific), 2mM Glutamine,

1 mM sodium Pyruvate, 0.1Mm NEAA, 0.05 mM β-mercaptoethanol, 100 U/ml Penicillin/Streptomycin supplemented with N-2 Supplement 100X (175020, ThermoFisher Scientific), and B-27 Supplement minus Vitamin A 50X (125870, ThermoFisher Scientific). The protocol of ES neuralization consisted of three steps. In the first step, dissociated ES cells were washed with DMEM/F12, seeded on gelatin-coated culture dishes (65000 cells per cm^2) and kept for 24 hours in 2i + LIF medium. The day after (DIV0), medium is changed to CDMM plus 2.5 μM 53AH Wnt inhibitor (C5324-10, Cellagen Technology) and 0.25 μM of the BMP inhibitor LDN193189 hydrochloride (SML0559, Sigma Aldrich), for 3 days, until DIV3. At this point (start of Step 2), ES cells were dissociated and seeded (65000 cells per cm^2) on Poly-ornithine (P3655 Sigma-Aldrich; 20 μg/ml in sterile water, 24 hours coating at 37°C) and natural mouse Laminin (23017015, ThermoFisher Scientific; 2.5 μg/ml in PBS, 24 hours coating at 37°C). Cells were cultured for 4 additional days (until DIV7) in CDMM Plus Wnt/BMP inhibitors, changing the medium daily. Serum employed for Trypsin inactivation was carefully removed by several washes in DMEM/F12. At DIV7, cells were dissociated and seeded (125000 cells per cm^2) on Poly-ornithine and Laminin coated wells. Subsequently, isocortical culture were kept in CDMM Plus Wnt/BMP inhibitors from DIV7 to DIV22 (StepIII). On

the eleventh day of Step III, DMEM/F12 was replaced with Neurobasal B27 and NEAA were removed from the CDMM to avoid glutamate-induced excitotoxicity. Medium was changed daily until the next step.

ii. Plasmids and cell transfections

CD63-pEGFP C2 was a gift from Paul Luzio (Addgene plasmid # 62964); LAMP1-mGFP was a gift from Esteban Dell'Angelica (Addgene plasmid # 34831); pEGFP-N3 was a gift from Vincenzo Sorrentino (University of Siena). Lipid-based transfection of plasmidic DNA was performed using Lipofectamine® 2000 transfection reagent (Invitrogen, Carlsbad, CA). In order to obtain DNA-lipid complexes for each dish 2 µg of plasmidic DNA were mixed with 6 µL of Lipofectamine. Before complexation, plasmidic DNA and Lipofectamine were diluted with Optimem® (Invitrogen, Carlsbad, CA) in order to have a volume of 100 µL. After an incubation time of 5 min at room temperature, the DNA-lipid complexes were added to the cells. Cells were incubated with complexes either for 4 h or for 24 h at 37° and used in experiment. Transfection by electroporation was carried out using Neon Transfection System 10 µL Kit (Invitrogen, Carlsbad, CA). Cells were trypsinized, pelleted, and resuspended in Resuspension Buffer R. The

electroporation was performed using 5×10^5 cells per reaction in 10 µL buffer containing plasmidic DNA at the concentration of 0.1 µg/µL, operating two pulses at a voltage of 1005 V and width of 35 ms. The cells were then seeded and cultured in DMEM containing 10% FBS and supplements without antibiotics and used in experiments 24 h later.

CellLight® Lysosomes-GFP, BacMam 2.0 (ThermoFisher Scientific), was used as additional method to obtain lysosomes labelled with GFP-tagged LAMP1.

Nonliposomal lipid-based transfection was carried out using Effectene® Transfection Reagent (QIAGEN). Briefly, for each dish 0.4 µg of plasmidic DNA dissolved in Buffer EC were mixed with 3.2 µL of Enhancer. 10 µL of Effectene Trasfection Reagent were mixed to the DNA solution and incubated for 10 min at room temperature to allow transfection-complex formation. Cells were incubated with complexes under their normal growth conditions for 24h for expression of the transfected gene.

Finally, for stable transfection, HeLa cells were transfected by electroporation, as previously described, with CD63-EGFP and LAMP1-GFP constructs, both carrying NeoR gene which confers resistance to Geneticin (G418). After 48 h of culture, the medium was

replaced with fresh complete medium supplemented with G418 at 2 mg/mL and a 12 days selection allowed obtaining a stable polyclonal cell population expressing fluorescent CD63 or LAMP1. After selection, G418 concentration was reduced at 0.5 mg/mL as maintenance medium for 1 week. The day before experiment, 2×10^5 stably transfected cells were seeded onto each Willco dish in complete medium devoid of G148, and were analyzed at the confocal microscope 24h later.

iii. Live cell imaging

Confocal fluorescence image series for the dynamic fingerprinting of sub-cellular nanostructures by *i*MSD analysis were acquired with an Olympus FluoView FV1000 confocal microscope with a 60x NA 1.20 water immersion objective. All experiments were carried out at 37 °C and 5% CO_2 using an incubation chamber enclosing the microscope stage and body. 488 nm Argon laser was used for excitation of early/late endosomes, caveolae, macropinosomes and clathrin-coated vesicles. The fluorescence emission was collected between 500 and 600 nm with the PMT detector in analog mode. 543 nm laser was used to excite Lysotracker. In this case, fluorescence emission was

collected between 555 and 655 nm with the PMT detector in analog mode. The diameter of the detection pinhole was set to the size of 1 Airy. Sequential image series at 16 bits were collected at a fixed pixel size of 69 nm selecting a region of interest of 256 × 256 pixels and by varying the pixel dwell time from 0.5 to 2 or 4 µs per pixel depending on the characteristic diffusivity of the structure under study. The overall acquisition time varied from 30 seconds to 10 minutes, depending on the application.

Confocal fluorescence image series for all the other analysis were acquired with a Leica SP5 confocal microscope with a 100× NA 1.30 oil immersion objective. All experiments were carried out at 37 °C and 5% CO_2 using an incubation chamber enclosing the microscope stage and body and a smaller chamber around the sample for CO_2 control. A 561 nm DPSS laser was used to excite LysoTracker® Red DND-99. Fluorescence emission was collected in the 570–670 nm range, with the PMT detector working in analog mode. The diameter of the detection pinhole was set to the standard size of 1 Airy. Sequential image series of 1300 frames at 8 bits were collected at a fixed pixel size of 67.5 nm selecting a region of interest of 256 × 256 pixels. The scan speed was set to the frequency of 1400 Hz, with a resulting frame

time interval of 112 ms. The overall acquisition time was of approximately 145 s.

Bibliography

1. Bruce Alberts, Alexander Johnson, Julian Lewis, Martin Raff, Keith Roberts, and P. W. Alberts - Molecular Biology Of The Cell 4th Ed. *J. Chem. Inf. Model.* **53**, 160 (2002).

2. Callaway, E. Cell transport carries off nobel. *Nature* **502**, 149–150 (2013).

3. Murphy, J. E., Padilla, B. E., Hasdemir, B., Cottrell, G. S. & Bunnett, N. W. Endosomes: A legitimate platform for the signaling train. *Proceedings of the National Academy of Sciences of the United States of America* **106**, 17615–17622 (2009).

4. Mellman, I. & Yarden, Y. Endocytosis and cancer. *Cold Spring Harb. Perspect. Biol.* **5**, (2013).

5. Mosesson, Y., Mills, G. B. & Yarden, Y. Derailed endocytosis: An emerging feature of cancer. *Nature Reviews Cancer* **8**, 835–850 (2008).

6. Di Fiore, P. P. Endocytosis, signaling and cancer, much more than meets the eye. *Molecular Oncology* **3**, 273–279 (2009).

7. Castermans, D. *et al.* SCAMP5, NBEA and AMISYN: Three candidate genes for autism involved in secretion of large dense-core vesicles. *Hum. Mol. Genet.* **19**, 1368–1378 (2010).

8. Johnson, R. D., Oliver, P. L. & Davies, K. E. *SNARE proteins and schizophrenia: linking synaptic and neurodevelopmental hypotheses*. (2008).

9. Bogan, J. S. Regulation of glucose transporter translocation in

health and diabetes. *Annu. Rev. Biochem.* **81**, 507–532 (2012).

10. Janka, G. E. Familial and acquired hemophagocytic lymphohistiocytosis. *Annual Review of Medicine* **63**, 233–246 (2012).

11. Khoriaty, R., Vasievich, M. P. & Ginsburg, D. The COPII pathway and hematologic disease. *Blood* **120**, 31–38 (2012).

12. Bright, N. A., Gratian, M. J. & Luzio, J. P. Endocytic delivery to lysosomes mediated by concurrent fusion and kissing events in living cells. *Curr. Biol.* **15**, 360–365 (2005).

13. Li, X. *et al.* A molecular mechanism to regulate lysosome motility for lysosome positioning and tubulation. *Nat. Cell Biol.* **18**, 404–417 (2016).

14. Bandyopadhyay, D., Cyphersmith, A., Zapata, J. A., Kim, Y. J. & Payne, C. K. Lysosome transport as a function of lysosome diameter. *PLoS One* **9**, 18–23 (2014).

15. Di Rienzo, C., Gratton, E., Beltram, F. & Cardarelli, F. Fast spatiotemporal correlation spectroscopy to determine protein lateral diffusion laws in live cell membranes. *Proc. Natl. Acad. Sci.* **110**, 12307–12312 (2013).

16. Di Rienzo, C., Gratton, E., Beltram, F. & Cardarelli, F. Super-resolution in a standard microscope: From fast fluorescence imaging to molecular diffusion laws in live cells. in *Taylor & Francis Group* 19–47 (2016). doi:10.1201/9781315371627

17. Digiacomo, L., Digman, M. A., Gratton, E. & Caracciolo, G. Development of an image Mean Square Displacement (iMSD)-based method as a novel approach to study the intracellular trafficking of nanoparticles. *Acta Biomater.* **42**, 189–198

(2016).

18. Bogan, J. S., Xu, Y. & Hao, M. Cholesterol Accumulation Increases Insulin Granule Size and Impairs Membrane Trafficking. *Traffic* **13**, 1466–1480 (2012).

19. Ballabio, A. & Gieselmann, V. Lysosomal disorders: From storage to cellular damage. *Biochim. Biophys. Acta - Mol. Cell Res.* **1793**, 684–696 (2009).

20. Hu, Y. B., Dammer, E. B., Ren, R. J. & Wang, G. The endosomal-lysosomal system: From acidification and cargo sorting to neurodegeneration. *Translational Neurodegeneration* **4**, (2015).

21. Scipioni, L., Gratton, E., Diaspro, A. & Lanzanò, L. Phasor Analysis of Local ICS Detects Heterogeneity in Size and Number of Intracellular Vesicles. *Biophys. J.* **111**, 619–629 (2016).

22. Li, C. H., Bai, L., Li, D. D., Xia, S. & Xu, T. Dynamic tracking and mobility analysis of single GLUT4 storage vesicle in live 3T3-L1 cells. *Cell Res.* **14**, 480–486 (2004).

23. Donovan, K. W. & Bretscher, A. Tracking individual secretory vesicles during exocytosis reveals an ordered and regulated process. *J. Cell Biol.* **210**, 181–189 (2015).

24. Westphal, V. *et al.* Video-rate far-field optical nanoscopy dissects synaptic vesicle movement. *Science (80-.).* **320**, 246–249 (2008).

25. Tabei, S. M. A. *et al.* Intracellular transport of insulin granules is a subordinated random walk. *Proc. Natl. Acad. Sci. U. S. A.* **110**, 4911–4916 (2013).

26. Bálint, Š., Vilanova, I. V., Álvarez, Á. S. & Lakadamyali, M. Correlative live-cell and superresolution microscopy reveals cargo transport dynamics at microtubule intersections. *Proc. Natl. Acad. Sci. U. S. A.* **110**, 3375–3380 (2013).

27. Cardarelli, F. *et al.* The intracellular trafficking mechanism of Lipofectamine-based transfection reagents and its implication for gene delivery. *Sci. Rep.* **6**, 1–8 (2016).

28. MF, D. Zinc-ligand interactions modulate assembly and stability of the insulin hexamer -- a review. *Biometals* **18**, 295–303 (2005).

29. Nam, D., Mantell, J., Bull, D., Verkade, P. & Achim, A. A Novel Framework for Segmentation of Secretory Granules in Electron Micrographs. *Med. Image Anal.* **18**, 411–424 (2014).

30. Hurbain, I., Romao, M., Bergam, P., Heiligenstein, X. & Raposo, G. Analyzing lysosome-related organelles by electron microscopy. in *Methods in Molecular Biology* **1594**, 43–71 (Humana Press Inc., 2017).

31. Abbe, E. Beiträge zur Theorie des Mikroskops und der mikroskopischen Wahrnehmung: I. Die Construction von Mikroskopen auf Grund der Theorie. *Arch. für mikroskopische Anat.* **9**, 413–418 (1873).

32. Rust, M. J., Bates, M. & Zhuang, X. Sub-diffraction-limit imaging by stochastic optical reconstruction microscopy (STORM). *Nat. Methods* **3**, 793 (2006).

33. Betzig, E. *et al.* Imaging Intracellular Fluorescent Proteins at Nanometer Resolution. *Science (80-.).* **313**, 1642–1645 (2006).

34. Hess, S. T., Girirajan, T. P. K. & Mason, M. D. Ultra-high resolution imaging by fluorescence photoactivation localization microscopy. *Biophys. J.* **91**, 4258–4272 (2006).

35. Huang, B., Bates, M. & Zhuang, X. Super-resolution fluorescence microscopy. *Annual Review of Biochemistry* **78**, 993–1016 (2009).

36. Huang, B., Wang, W., Bates, M. & Zhuang, X. Three-dimensional super-resolution imaging by stochastic optical reconstruction microscopy. *Science (80-.).* **319**, 810–813 (2008).

37. Xu, J., Ma, H. & Liu, Y. Stochastic optical reconstruction microscopy (STORM). *Curr. Protoc. Cytom.* **2017**, 12.46.1-12.46.27 (2017).

38. Cox, S. Super-resolution imaging in live cells. *Developmental Biology* **401**, 175–181 (2015).

39. Cox, S. & Jones, G. E. *Imaging cells at the nanoscale*. **45**, 1669–1678 (2013).

40. Manley, S. *et al.* High-density mapping of single-molecule trajectories with photoactivated localization microscopy. *Nat. Methods 2008 52* **5**, 155–157 (2008).

41. Hell, S. W. & Wichmann, J. Breaking the diffraction resolution limit by stimulated emission: stimulated-emission-depletion fluorescence microscopy. *Opt. Lett.* **19**, 780 (1994).

42. Honigmann, A. *et al.* ARTICLE Scanning STED-FCS reveals spatiotemporal heterogeneity of lipid interaction in the plasma membrane of living cells. (2014). doi:10.1038/ncomms6412

43. Blom, H. & Widengren, J. Stimulated Emission Depletion

Microscopy. *Chem. Rev.* **117**, 7377–7427 (2017).

44. Schneider, J. *et al.* Ultrafast, temporally stochastic STED nanoscopy of millisecond dynamics. *Nat. Methods* **12**, 827–830 (2015).

45. Manzo, C. & Garcia-Parajo, M. F. A review of progress in single particle tracking: From methods to biophysical insights. *Reports on Progress in Physics* **78**, 124601 (2015).

46. Elson, E. L. & Magde, D. Fluorescence correlation spectroscopy. I. Conceptual basis and theory. *Biopolymers* **13**, 1–27 (1974).

47. Ries, J. Advanced Fluorescence Correlation Techniques to Study Membrane Dynamics. *PhD Thesis* (2008).

48. Meacci, G. *et al.* Mobility of Min-proteins in Escherichia coli measured by fluorescence correlation spectroscopy. *Phys. Biol.* **3**, 255–263 (2006).

49. Bacia, K., Scherfeld, D., Kahya, N. & Schwille, P. Fluorescence correlation spectroscopy relates rafts in model and native membranes. *Biophys. J.* **87**, 1034–1043 (2004).

50. Kahya, N. & Schwille, P. Fluorescence correlation studies of lipid domains in model membranes (Review). *Molecular Membrane Biology* **23**, 29–39 (2006).

51. Bates, I. R., Wiseman, P. W. & Hanrahan, J. W. Investigating membrane protein dynamics in living cells. in *Biochemistry and Cell Biology* **84**, 825–831 (Biochem Cell Biol, 2006).

52. Petrášek, Z., Ries, J. & Schwille, P. Scanning FCS for the Characterization of Protein Dynamics in Live Cells. in *Methods in Enzymology* **472**, 317–343 (Academic Press,

2010).

53. Dertinger, T. *et al.* Two-focus fluorescence correlation spectroscopy: A new tool for accurate and absolute diffusion measurements. *ChemPhysChem* **8**, 433–443 (2007).

54. Digman, M. A. *et al.* Measuring fast dynamics in solutions and cells with a laser scanning microscope. *Biophys. J.* **89**, 1317–1327 (2005).

55. Ruan, Q., Cheng, M. A., Levi, M., Gratton, E. & Mantulin, W. W. Spatial-temporal studies of membrane dynamics: Scanning fluorescence correlation spectroscopy (SFCS). *Biophys. J.* **87**, 1260–1267 (2004).

56. Petrášek, Z. & Schwille, P. Precise measurement of diffusion coefficients using scanning fluorescence correlation spectroscopy. *Biophys. J.* **94**, 1437–1448 (2008).

57. Petrášek, Z. & Schwille, P. Scanning Fluorescence Correlation Spectroscopy. in 83–105 (Springer, Berlin, Heidelberg, 2008). doi:10.1007/978-3-540-73924-1_4

58. Digman, M. A. & Gratton, E. Analysis of diffusion and binding in cells using the RIGS approach. *Microsc. Res. Tech.* **72**, 323–332 (2009).

59. Digman, M. A. *et al.* Fluctuation correlation spectroscopy with a laser-scanning microscope: Exploiting the hidden time structure. *Biophys. J.* **88**, L33–L36 (2005).

60. Di Rienzo, C., Piazza, V., Gratton, E., Beltram, F. & Cardarelli, F. Probing short-range protein Brownian motion in the cytoplasm of living cells. *Nat. Commun.* **5**, 1–8 (2014).

61. Hebert, B., Costantino, S. & Wiseman, P. W. Spatiotemporal

image correlation spectroscopy (STICS) theory, verification, and application to protein velocity mapping in living CHO cells. *Biophys. J.* **88**, 3601–3614 (2005).

62. Brown, C. M. *et al.* Raster image correlation spectroscopy (RICS) for measuring fast protein dynamics and concentrations with a commercial laser scanning confocal microscope. *J. Microsc.* **229**, 78–91 (2008).

63. Sako, Y. & Kusumi, A. Barriers for lateral diffusion of transferrin receptor in the plasma membrane as characterized by receptor dragging by laser tweezers: Fence versus tether. *J. Cell Biol.* **129**, 1559–1574 (1995).

64. Fujiwara, T., Ritchie, K., Murakoshi, H., Jacobson, K. & Kusumi, A. Phospholipids undergo hop diffusion in compartmentalized cell membrane. *J. Cell Biol.* **157**, 1071–1081 (2002).

65. Huisken, J. & Stainier, D. Y. R. Selective plane illumination microscopy techniques in developmental biology. *Development* **136**, 1963–1975 (2009).

66. Li, D. *et al.* Extended-resolution structured illumination imaging of endocytic and cytoskeletal dynamics. *Science (80-.).* **349**, aab3500–aab3500 (2015).

67. Magidson, V. & Khodjakov, A. Circumventing photodamage in live-cell microscopy. in *Methods in Cell Biology* **114**, 545–560 (Academic Press Inc., 2013).

68. Saftig, P. & Klumperman, J. Lysosome biogenesis and lysosomal membrane proteins: Trafficking meets function. *Nat. Rev. Mol. Cell Biol.* **10**, 623–635 (2009).

69. Appelqvist, H., Wäster, P., Kågedal, K. & Öllinger, K. The lysosome: from waste bag to potential therapeutic target. *J. Mol. Cell Biol.* **5**, 214–226 (2013).

70. Ballabio, A. The awesome lysosome. *EMBO Mol. Med.* **8**, 73–76 (2016).

71. Settembre, C., Fraldi, A., Medina, D. L. & Ballabio, A. Signals from the lysosome: a control centre for cellular clearance and energy metabolism. *Nat. Rev. Mol. Cell Biol.* **14**, 283–296 (2013).

72. Napolitano, G. & Ballabio, A. TFEB at a glance. *J. Cell Sci.* **129**, 2475–81 (2016).

73. Wan, X. *et al.* Pancreatic islets communicate with lymphoid tissues via exocytosis of insulin peptides. *Nature* 1 (2018). doi:10.1038/s41586-018-0341-6

74. Collot, M., Louvard, D. & Singer, S. J. Lysosomes are associated with microtubules and not with intermediate filaments in cultured fibroblasts. *Proc. Natl. Acad. Sci. U. S. A.* **81**, 788–792 (1984).

75. Mithieux, G. & Rousset, B. Identification of a lysosome membrane protein which could mediate ATP-dependent stable association of lysosomes to microtubules. *J. Biol. Chem.* **264**, 4664–4668 (1989).

76. Cordonnier, M. N., Dauzonne, D., Louvard, D. & Coudrier, E. Actin filaments and myosin I alpha cooperate with microtubules for the movement of lysosomes. *Mol. Biol. Cell* **12**, 4013–4029 (2001).

77. Swanson, J. A. & Watts, C. Macropinocytosis. *Trends in Cell*

Biology **5**, 424–428 (1995).

78. McMahon, H. T. & Boucrot, E. Molecular mechanism and physiological functions of clathrin-mediated endocytosis. *Nature Reviews Molecular Cell Biology* **12**, 517–533 (2011).

79. Predescu, S. A., Predescu, D. N. & Malik, A. B. Molecular determinants of endothelial transcytosis and their role in endothelial permeability. *American Journal of Physiology - Lung Cellular and Molecular Physiology* **293**, (2007).

80. Gaidarov, I., Santini, F., Warren, R. A. & Keen, J. H. Spatial control of coated-pit dynamics in living cells. *Nat. Cell Biol.* **1**, 1–7 (1999).

81. Wang, Z., Tiruppathi, C., Minshall, R. D. & Malik, A. B. Size and dynamics of caveolae studied using nanoparticles in living endothelial cells. *ACS Nano* **3**, 4110–4116 (2009).

82. Jones, A. T. Macropinocytosis: Searching for an endocytic identity and role in the uptake of cell penetrating peptides. *Journal of Cellular and Molecular Medicine* **11**, 670–684 (2007).

83. Piper, R. C. & Luzio, J. P. Late endosomes: Sorting and partitioning in multivesicular bodies. *Traffic* **2**, 612–621 (2001).

84. Rink, J., Ghigo, E., Kalaidzidis, Y. & Zerial, M. Rab conversion as a mechanism of progression from early to late endosomes. *Cell* **122**, 735–749 (2005).

85. Falcone, S. *et al.* Macropinocytosis: Regulated coordination of endocytic and exocytic membrane traffic events. *J. Cell Sci.* **119**, 4758–4769 (2006).

86. Kerr, M. C. *et al.* Visualisation of macropinosome maturation by the recruitment of sorting nexins. *J. Cell Sci.* **119**, 3967–3980 (2006).

87. Digiacomo, L. *et al.* Dynamic fingerprinting of sub-cellular nanostructures by image mean square displacement analysis. *Sci. Rep.* **7**, 14836 (2017).

88. Ferri, G. *et al.* Time-lapse confocal imaging datasets to assess structural and dynamic properties of subcellular nanostructures. *Sci. Data* **5**, 1–8 (2018).

89. Pryor, P. R. *Analyzing lysosomes in live cells*. *Methods in Enzymology* **505**, (Elsevier Inc., 2012).

90. Albers; Johnson; Lewis; Raff; Roberts; Walter. *Molecular biology of The Cell*. (Garland Science, 2002).

91. Ihrke, G., Kyttälä, A., Russell, M. R. G., Rous, B. a & Luzio, J. P. Differential use of two AP-3-mediated pathways by lysosomal membrane proteins. *Traffic* **5**, 946–962 (2004).

92. Shapiro, J. L. *et al.* Cellular uptake of amelogenin, and its localization to CD63, and Lamp1-positive vesicles. *Cell. Mol. Life Sci.* **64**, 244–256 (2007).

93. Rosa-Ferreira, C. & Munro, S. Arl8 and SKIP Act Together to Link Lysosomes to Kinesin-1. *Dev. Cell* **21**, 1171–1178 (2011).

94. Cook, N. R., Row, P. E. & Davidson, H. W. Lysosome associated membrane protein 1 (Lamp1) traffics directly from the TGN to early endosomes. *Traffic* **5**, 685–699 (2004).

95. Schwake, M., Schröder, B. & Saftig, P. Lysosomal Membrane Proteins and Their Central Role in Physiology. *Traffic* **14**, 739–

748 (2013).

96. Pols, M. S. & Klumperman, J. Trafficking and function of the tetraspanin CD63. *Exp. Cell Res.* **315**, 1584–1592 (2009).

97. Wei, J. & Yewdell, J. W. Peptide secretion triggers diabetes. *Nature* (2018). doi:10.1038/d41586-018-05710-z

98. Bertacchi, M., Pandolfini, L., D'Onofrio, M., Brandi, R. & Cremisi, F. The double inhibition of endogenously produced bmp and wnt factors synergistically triggers dorsal telencephalic differentiation of mouse es cells. *Dev. Neurobiol.* **75**, 66–79 (2015).

99. Afroze, S. H. *et al.* Liver Regeneration. The Stem Cell Approach. in *Regenerative Medicine Applications in Organ Transplantation* 375–390 (Elsevier Inc., 2014). doi:10.1016/B978-0-12-398523-1.00026-4

100. Tropepe, V. *et al.* Direct neural fate specification from embryonic stem cells: A primitive mammalian neural stem cell stage acquired through a default mechanism. *Neuron* **30**, 65–78 (2001).

101. Smukler, S. R., Runciman, S. B., Xu, S. & Van Der Kooy, D. Embryonic stem cells assume a primitive neural stem cell fate in the absence of extrinsic influences. *J. Cell Biol.* **172**, 79–90 (2006).

102. Shimogori, T., Banuchi, V., Ng, H. Y., Strauss, J. B. & Grove, E. A. Embryonic signaling centers expressing BMP, WNT and FGF proteins interact to pattern the cerebral cortex. *Development* **131**, 5639–5647 (2004).

103. Lupo, G. *et al.* From pluripotency to forebrain patterning: An

in vitro journey astride embryonic stem cells. *Cell. Mol. Life Sci.* **71**, 2917–2930 (2014).

104. Boergermann, J. H., Kopf, J., Yu, P. B. & Knaus, P. Dorsomorphin and LDN-193189 inhibit BMP-mediated Smad, p38 and Akt signalling in C2C12 cells. *Int. J. Biochem. Cell Biol.* **42**, 1802–1807 (2010).

105. Ferguson, S. M. Axonal transport and maturation of lysosomes. *Current Opinion in Neurobiology* **51**, 45–51 (2018).

106. Vukoja, A. *et al.* Presynaptic Biogenesis Requires Axonal Transport of Lysosome-Related Vesicles. *Neuron* **99**, 1216-1232.e7 (2018).

107. Nozumi, M., Nakatsu, F., Katoh, K. & Igarashi, M. Coordinated Movement of Vesicles and Actin Bundles during Nerve Growth Revealed by Superresolution Microscopy. *Cell Rep.* **18**, 2203–2216 (2017).

108. Marchetti, L. *et al.* Ligand-induced dynamics of neurotrophin receptors investigated by single-molecule imaging approaches. *Int. J. Mol. Sci.* **16**, 1949–1979 (2015).

109. De Nadai, T. *et al.* Precursor and mature NGF live tracking: One versus many at a time in the axons. *Sci. Rep.* **6**, (2016).

110. Marchetti, L. *et al.* Ligand signature in the membrane dynamics of single TrkA receptor molecules. *J. Cell Sci.* **126**, 4445–4456 (2013).

111. Callegari, A. *et al.* Single particle tracking of acyl carrier protein (ACP)-tagged TrkA receptors in PC12nnr5 cells. *Journal of Neuroscience Methods* **204**, 82–86 (2012).

112. Amodeo, R. *et al.* Molecular insight on the altered membrane trafficking of TrkA kinase dead mutants. *Biochim. Biophys. Acta - Mol. Cell Res.* **1867**, (2020).

113. Liu, P. *et al.* Histone deacetylation promotes mouse neural induction by restricting Nodal-dependent mesendoderm fate. *Nat. Commun.* **6**, 1–14 (2015).

114. Ying, Q. L., Stavridis, M., Griffiths, D., Li, M. & Smith, A. Conversion of embryonic stem cells into neuroectodermal precursors in adherent monoculture. *Nat. Biotechnol.* **21**, 183–186 (2003).

115. Abranches, E. *et al.* Neural differentiation of embryonic stem cells in vitro: A road map to neurogenesis in the embryo. *PLoS One* **4**, (2009).

116. Convertino, D. *et al.* Graphene promotes axon elongation through local stall of Nerve Growth Factor signaling endosomes. *Nano Lett.* acs.nanolett.0c00571 (2020). doi:10.1021/acs.nanolett.0c00571

117. Gobbo, F. *et al.* Activity-dependent expression of Channelrhodopsin at neuronal synapses. *Nat. Commun.* **8**, (2017).

118. Liao, Y.-C. *et al.* RNA Granules Hitchhike on Lysosomes for Long-Distance Transport, Using Annexin A11 as a Molecular Tether. *Cell* **179**, 147-164.e20 (2019).

119. Digman, M. A., Dalal, R., Horwitz, A. F. & Gratton, E. Mapping the number of molecules and brightness in the laser scanning microscope. *Biophys. J.* **94**, 2320–2332 (2008).

120. Caracciolo, G., Farokhzad, O. C. & Mahmoudi, M. Biological

Identity of Nanoparticles In Vivo: Clinical Implications of the Protein Corona. *Trends in Biotechnology* **35**, 257–264 (2017).

121. Palchetti, S. *et al.* Manipulation of lipoplex concentration at the cell surface boosts transfection efficiency in hard-to-transfect cells. *Nanomedicine Nanotechnology, Biol. Med.* **13**, 681–691 (2017).

122. Di Rienzo, C., Gratton, E., Beltram, F. & Cardarelli, F. Spatiotemporal Fluctuation Analysis: A Powerful Tool for the Future Nanoscopy of Molecular Processes. *Biophys. J.* **111**, 679–685 (2016).

123. Jain, M. & Jesus, O. De. Krabbe Disease. *StatPearls* (2021).

124. De Gasperi, R. *et al.* Transgenic rescue of Krabbe disease in the twitcher mouse. *Gene Ther.* **11**, 1188–1194 (2004).

125. Devany, J., Chakraborty, K. & Krishnan, Y. Subcellular Nanorheology Reveals Lysosomal Viscosity as a Reporter for Lysosomal Storage Diseases. *Nano Lett.* **18**, 1351–1359 (2018).

Acknowledgements

Throughout the writing of this dissertation I have received a great deal of support and assistance.

I would like to thank my supervisor, Prof. Francesco Cardarelli, for providing guidance and feedback throughout this project. His expertise was invaluable in formulating the research questions and methodology which pushed me to sharpen my thinking and brought my work to a higher level. I would also like to acknowledge Prof. Fabio Beltram, for giving me the opportunity to work at NEST research center, Prof. Stefano Luin and Dr. Laura Marchetti for their precious contribution to my project.

I would like to extend my sincere thanks to my colleagues and research team – Francesca D'Autilia, Gianmarco Ferri, Manuella Martins, Rosy Amodeo and Carmine di Rienzo - for a cherished time spent together in the lab.

In addition, I would like to thank my family who gave me the chance to study and my friend Giuseppe who encouraged me all through my studies. Finally, my biggest thanks to Cinzia for her unwavering support and belief in me.